

149600-1-f

AD A115099

UNCLASSIFIED

ADF 200-02-

(2)

Final Report

# REMOTE BATHYMETRY WITH A MULTISPECTRAL ACTIVE/PASSIVE AIRBORNE SYSTEM

D.R. LYZENGA, J.S. OTT, J.P. LIVISAY, F.C. POLCYN  
Applications Division

FEBRUARY 1982

Contract No. N61331-80-C-0022  
Technical Monitor Mr. Mike Cooper

Approved for Public Release:  
Distribution Unlimited



Naval Coastal Systems Center  
Panama City, Florida 32407

DTIC  
ELECTRONIC  
S JUN 3 1982  
A

ENVIRONMENTAL  
**RESEARCH INSTITUTE OF MICHIGAN**  
BOX 8610 • ANN ARBOR • MICHIGAN 48107

COPY

SECURITY CLASSIFICATION OF THIS PAGE (If Data Entered)

REPORT DOCUMENTATION PAGE		READ INSTRUCTIONS BEFORE COMPLETING FORM
1. REPORT NUMBER 149600-1-F	2. GOVT ACCESSION NO <i>AD-H15 099</i>	3. RECIPIENT'S CATALOG NUMBER
4. TITLE (and Subtitle) Remote Bathymetry with a Multispectral Active/Passive Airborne System		5. TYPE OF REPORT & PERIOD COVERED Final Report 1980 - May 1981
7. AUTHOR(S) D.R. Lyzenga, J.S. Ott, J.P. Livisay, F.C. Polcyn		6. PERFORMING ORG REPORT NUMBER 149600-1-F 8. CONTRACT OR GRANT NUMBER(s) N61331-80-C-0022
9. PERFORMING ORGANIZATION NAME AND ADDRESS Environmental Research Institute of Michigan Applications Division, Box 8618 Ann Arbor, Michigan 48107		10. PROGRAM ELEMENT, PROJECT, TASK AREA & WORK UNIT NUMBERS
11. CONTROLLING OFFICE NAME AND ADDRESS Naval Coastal Systems Center Code 772 Panama City, FL 32407		12. REPORT DATE <i>May 1981</i> 13. NUMBER OF PAGES
14. MONITORING AGENCY NAME AND ADDRESS (if different from Controlling Office)		15. SECURITY CLASS (of this report) Unclassified 15A. DECLASSIFICATION/DOWNGRADING SCHEDULE
16. DISTRIBUTION STATEMENT (of this Report)  <div style="border: 1px solid black; padding: 5px; text-align: center;">This document has been approved for public release and sale; its distribution is unlimited.</div>		
17. DISTRIBUTION STATEMENT (of the abstract entered in Block 20, if different from Report)		
18. SUPPLEMENTARY NOTES		
19. KEY WORDS (Continue on reverse side if necessary and identify by block number) Remote Sensing      Bahama Bathymetry      Multispectral Lidar		
20. ABSTRACT (Continue on reverse side if necessary and identify by block number) Active/passive multispectral data collected at 1000 ft to 10,000 ft altitudes in the Bahamian Calibration Area were processed in order to construct bathymetric charts and images of the bottom reflectance. Preprocessing methods were developed to correct for sunglint and atmospheric attenuation effects as a function of scan angle. While depth charts can be made with ship measured control points as well as band ratio techniques, lidar time differences measured at 1000 ft altitude were found to be the best source of water depth (con't).		

DD FORM 1 JAN 73 1473 EDITION OF 1 NOV 65 IS OBSOLETE

SECURITY CLASSIFICATION OF THIS PAGE (If Data Entered)

SECURITY CLASSIFICATION OF THIS PAGE (When Data Entered)

20. calibration input data needed to identify parameters for extrapolation of water depth measuring techniques to higher altitudes.

SECURITY CLASSIFICATION OF THIS PAGE (When Data Entered)

## PREFACE

This report is submitted by the Environmental Research Institute of Michigan in fulfillment of the requirements for Contract N61331-80-C-0022 under sponsorship of the Naval Coastal Systems Center. The Contracting Officer's Technical Representative was Mr. Mike Cooper.

Color coded depth charts constructed from the remotely sensed data at scales previously agreed upon have been submitted separately to the Naval Coastal Systems Center.

The authors wish to acknowledge the assistance of James Hammack and John Spinning of the Defense Mapping Agency for providing the supporting data from the Bahamas Photobathymetric Calibration Area.

At ERIM, the assistance of Steve Stewart, Jimmie Ladd, William Juodawlkis, Harvey Doss, James Ledbetter and D. Thompson in collecting the active/passive multispectral data in the Bahamas in 1978 is appreciated. Typing by Ms. Nancy J. Moon and Lisa Cool is gratefully acknowledged.



## TABLE OF CONTENTS

## PREFACE

LIST OF FIGURES . . . . .	iv
LIST OF TABLES . . . . .	vi
1. INTRODUCTION . . . . .	1
2. DATA SET DESCRIPTION . . . . .	3
3. PROCESSING METHODS . . . . .	7
3.1 Preprocessing . . . . .	7
3.2 Calibration . . . . .	9
3.2.1 Lidar Calibration . . . . .	10
3.2.2 Transfer of Lidar Calibration to High Altitude Data . . . . .	11
3.2.3 Calibration Using Ship Data . . . . .	13
3.2.4 Ratio Processing Without Surface Truth . . . . .	14
3.2.5 Calibration for Bottom Feature Processing . . . . .	15
3.3 Depth Processing . . . . .	16
3.4 Bottom Feature Processing . . . . .	17
4. DATA ANALYSIS AND PROCESSING . . . . .	19
4.1 North Cat Cay (1000 ft) . . . . .	19
4.2 Bimini (1000 ft) . . . . .	33
4.3 Great Isaac Island (1000 ft) . . . . .	43
4.4 Grand Bahama Island . . . . .	45
4.5 North Cat Cay (10,800' Run) . . . . .	55
4.6 Bimini (10,800' Run) . . . . .	63
4.7 Great Isaac and Rocky Heads (10,800' Runs) . . . . .	71
5. ERROR ANALYSIS . . . . .	83
6. CONCLUSIONS . . . . .	95
REFERENCES . . . . .	97

## LIST OF FIGURES

<u>FIGURE</u>	<u>TITLE</u>	<u>PAGE</u>
1a & b	Average deep-water signal in band C8 versus pixel number.	20
2	Scatter plot of sun glint signals in bands C8 and C2 over deep water.	22
3	Comparison of depths obtained from lidar and passive data for North Cat Cay, Run 3, 8/12/78, 0900.	23
4	Depth chart for the North Cat Cay area.	27
5	Scatter plot of $X_8$ versus $X_5$ over sand bottom near North Cat Cay.	30
6	Bottom reflectance chart for the North Cat Cay area.	31
7	Comparison of depths obtained from lidar and passive data for Bimini, Run 7, 8/12/78, 1600.	34
8	Depth chart for the Bimini area.	37
9	Scatter plot of $X_9$ versus $X_6$ over sand bottom near Moselle Bank, off Bimini.	39
10	Bottom reflectance chart for the Bimini area.	41
11	Imagery of Grand Bahama Island, Run 1, 8/13/78, 0900.	47
12	Measured depth versus calculated depth, Grand Bahama Island.	49
13	Depth versus signal for band C5.	51
14	Depth versus signal for band C8.	52
15	Depth versus signal for band A1.	53
16	Depth chart for the North Cat Cay area.	59
17	Bottom reflectance chart for the North Cat Cay area.	61
18	Depth chart for the Bimini area	67
19	Bottom reflectance chart for the Bimini area.	69
20	Depth chart for the Great Isaac area.	75
21	Bottom reflectance chart for the Great Isaac area.	77

**LIST OF FIGURES (Continued)**

<u>FIGURE</u>	<u>TITLE</u>	<u>PAGE</u>
22	Depth chart for the Rocky Heads area North of Mackie Shoal.	79
23	Bottom reflectance chart for the Rocky Heads area North of Mackie Shoal.	81
24	Depth error ( $\Delta Z$ ) versus bottom-type index (Y) versus scan line number for North Cat Cay data set.	86
25	Depth error ( $\Delta Z$ ) versus bottom-type index (Y) for North Cat Cay data set.	87
26	Depth error ( $\Delta Z$ ) and bottom-type index (Y) versus scan line number for Bimini data set.	89
27	Depth error ( $\Delta Z$ ) versus bottom-type index (Y) for Bimini data set.	90

**LIST OF TABLES**

<u>TABLE</u>	<u>TITLE</u>	<u>PAGE</u>
1	Data set description.	4
2	Comparison of signal statistics before and after sun glint correction (data records 1500-1600, points 250-300).	21
3	Depth correlation coefficients for various band pairs (North Cat Cay, sun glint corrected data).	24
4	Depth processing parameters for Bimini (1000 ft) data set.	33
5	Depth correlation coefficients for various band pairs (Bimini 1000 ft data set).	35
6	Depth correlation coefficients for various pairs (Great Isaac 1000 ft data set).	43
7	Comparison of signal statistics before and after sunglint correction (data records 700-800, points 280-400).	55
8	North Cat Cay (10,800' Run) ship buoy locations.	56
9	Processing parameters for high altitude passes.	58
10	Comparison of signal statistics before and after sunglint correction (data records 2-100, points 150-350).	63
11	Bimini (10,800' Run) ship buoy locations.	64
12	Sunglint parameters for Rocky Heads	71
13	Effects of sunglint correction.	72
14	Great Isaac and Rocky Heads 10,800' Run ship buoys Locations.	73
15	Comparison of calculated and observed depth errors for North Cat Cay and Bimini data sets.	85
16	Calculated depth errors for high altitude data sets.	91

## INTRODUCTION

During the summer of 1978, a series of data collection flights were conducted at the request of James Hammack and John Spinning of the Defense Mapping Agency in conjunction with their measurement program creating the Bahamas Photobathymetric Calibration area. Extensive ship surveys were made giving water depths as a function of known geographic position based on a Decca navigation grid set up by two slave stations positioned along the Florida coast with the master station carried aboard the survey ship. This basic set of data has become part of a continuing program to demonstrate and prove the accuracy of water depth measurements (remote bathymetry) made from satellite and aircraft platforms using the selective absorption of sunlight as the basis for calculating depth.

The passive multispectral system approach has been shown to give acceptable depth measurement when certain parameters are known a priori e.g., the bottom reflectance and the water attenuation coefficient.

The equation relating depth to various constants can also be solved for these two unknowns if the water depth is known at certain reference points. The use of an active laser pulse system (LIDAR) to give water depth by measuring the time difference of the signal reflected from the surface and bottom appears to be an attractive alternative for obtaining water depths at control points in the area. The objective of this effort reported herein was to compare the accuracies of the remote measurement of water depth when the two important input variables were either

- (1) assumed based on knowledge of the general area characteristics in the Bahamas;

- (2) measured by ship fathometer data as inputs to the remote depth equation; or
- (3) measured by the laser pulse time differences as the preferred method of calibrating the passive multispectral scanner.

An additional goal was to assess the ability of extrapolating the measurements of the two variables, bottom reflectance and water attenuation coefficient from those measured at 1000 ft aircraft altitude and using them to process depth data at 10,000 ft aircraft altitude and eventually spacecraft altitudes.

The active/passive multispectral airborne data has other uses, among them evaluation of bottom reflectances at variable picture element sizes, development of preprocessing techniques for angle correction and sun glint removal, and simulation of band locations or spectral band widths for future spaceborne systems.

## DATA SET DESCRIPTION

The sets of aircraft multispectral imagery used as the foundation of this study come from the Bahamas experiment of 1978 [1]. During that experiment imagery was collected over both the Great and Little Bahama Banks, at altitudes of 1000, 1500, and 10,800 feet. On the lower altitude flights the active/passive capability of the scanner was utilized to make lidar determinations of the shallow water depths. Data sets were selected from that experiment in order to evaluate the processing methodology used in making water depth charts, and the magnitude of the errors in the calculated depths due to factors such as noise, bottom reflectance variations, and water column optical properties.

The imagery selected for this investigation is summarized in Table 1. The four high altitude (10,800 ft) data sets and two low altitude (1000 ft) data sets were processed to provide water depth charts and bottom feature charts. Two other low altitude (1500 ft) data sets were used to correlate depths with thermal signals. Low altitude set #3 was used to provide the deep water calibration data for #4, and low altitude set #6 was processed to determine depth calibration constants for use with high altitude data.

Some of the conditions that influenced the choice of data sets were:

1. The existence of lidar data within the area of the high altitude imagery for depth calibration.
2. The existence of ship depth measurements in the high altitude imagery area.
3. Varied bottom reflectances in the high altitude imagery areas for adequate depth error evaluations.

TABLE 1  
DATA SET DESCRIPTION

<u>Data Set</u>	<u>Date</u>	<u>Time</u>	<u>Run</u>	<u>Altitude (ft)</u>	<u>Area</u>	<u>Heading</u>
1	8/12	1600	7	1,000	Bimini	NW
2	8/12	0900	7	10,800	Bimini	NE
3	8/12	0900	2	1,000	North Cat Cay	S
4	8/12	0900	3	1,000	North Cat cay	N
5	8/12	0900	5	10,800	North Cat Cay	N
6	8/12	1600	2	1,000	Great Isaac Island	W
7	8/12	1600	10	10,800	Great Isaac Island	E
8	8/12	1600	12	10,800	Rocky Heads	S
9	8/13	0900	11	1,500	Great Bahama Islands	E
10	8/13	0900	3	1,500	Great Bahama Islands	E

## DATA SET SPECTRAL BANDS

<u>Data Channel</u>	<u>Wavelength (μm)</u>
C2	.67-.94
C4	.62-.67
C5	.58-.64
C6	.55-.60
C7	.52-.57
C8	.50-.54
C9	.48-.52
A1	8.2-14.0

4. Water depth variations in the low altitude data to allow calibrations for depths ranging from 0 ft to 'deep water'.
5. Imagery of good quality, with minimum amounts of glint, haze, turbidity, etc.

In addition to the multispectral scanner (active/passive) data sets described above two other types of data were used to support the investigation, depth measurements made by ship and aerial photography [1]. The ship's procedure was to sail set courses, densely traversing areas of interest while automatically recording depth readings and position data. Buoys were distributed in areas that were selected for underwater reflectance measurements, and their positions recorded. These marked sites were photographed by aircraft [1] providing a way to establish location from geographical features.

There were two problem areas in the quality of the data that caused some concern during the course of the project.

1. Some of the early lidar measurements were hampered by spurious electronic anomalies, seriously affecting the processing for data sets 4, 6, 9, and 10.
2. The DECCA navigation system used by the ship to establish its position was not reliably operational at the time of the depth measurements. In many cases the ship positions as measured by the local Decca grid were inconsistent with the positions calculated with respect to the U.T.M. coordinate system especially when referencing the ship to fixed scene features.

### PROCESSING METHODS

The data sets described in section 2 were processed in order to generate water depth charts and bottom feature maps for the test areas. The processing methods used in this study are basically an elaboration of those described in Ref. 2, with certain modifications in the pre-processing steps as described in section 3.1, and with the inclusion of a new set of methods for calibrating the high altitude depth data as described in section 3.2. The general procedures for calibration and processing of the data are discussed in this section, and the specific results pertaining to each data set are described in section 4.

#### 3.1 PREPROCESSING

Data from the M-8 scanner are recorded on high density digital tape aboard the aircraft, with certain auxiliary information such as channel assignments and gain settings recorded manually on the flight data logs by the operating crew. The first step in processing this data is to copy selected portions of the high density tapes (HDTs) onto computer compatible tapes (CCTs). This step is carried out on the ERIM PDP-11/70 computer. The data is then transported via the CCTs to the University of Michigan Amdahl 470 computer for subsequent processing. This processing begins with an assessment and correction of artifacts such as scan angle and sun glint effects in the data, which, to distinguish them from the actual depth and bottom feature processing steps, are referred to as preprocessing steps.

Sun glint effects are evaluated by a statistical analysis of the signals over deep water, or if no deep water was encountered, over an area of uniform depth and bottom reflectance. Specifically, the correlation of these signals in the various spectral bands is investigated. If the correlation coefficient ( $r$ ) is low the sun glint is negligible, or at least not correctible, and processing continues with the evalua-

tion of scan angle effects. If the correlation coefficient is sufficiently high ( $r \geq 0.9$ ), this indicates that a significant amount of sun glint is present. A correction for this sun glint is obtained from the covariance  $\sigma_{ij}$  for channels  $i$  and  $j$ , where  $i$  is a visible channel used for depth processing and  $j$  is the near-infrared channel. Since the near-infrared channel does not penetrate the water to any significant depth, the only signal present over water is due to sun glint or atmospheric variations. Neglecting the latter, a correction for sun glint in channel  $i$  is given by

$$\Delta V_i = A_{ij} + B_{ij} V_j$$

where

$$A_{ij} = \bar{V}_i - (\sigma_{ij}/\sigma_{jj}) \bar{V}_j$$

and

$$B_{ij} = \sigma_{ij}/\sigma_{jj}$$

( $\bar{V}_i$  is the average deep-water signal in channel  $i$  in an area free of sun glint).  $\Delta V_i$  is calculated and subtracted from the raw signal  $V_i$  at each point in the scene. This procedure results in a significantly improved image if  $r$  is sufficiently large. A precise lower limit on the value of  $r$  for which an improvement is obtained by this procedure has not yet been established.

The second preprocessing step is an evaluation and correction of scan angle effects resulting from the wide scan angle ( $\pm 45^\circ$ ) of the M-8 scanner. In many cases, particularly at low altitude, the sun glint removal procedure described in the previous paragraph removes most of the angular variation of the signal. In other cases, however, a residual scan angle variation remains after the sun glint removal. This condition is detected by examining the angular dependence of the signal

over deep water after averaging in the along-track direction. A radiometric correction is made, if necessary, using the procedure described in reference 2 with one modification. This modification is to smooth the average scan line (from the computer program ACORN) before subtracting it from the rest of the data. This smoothing reduces the amount of along-path striping in the corrected data by removing noise spikes in the average scan line. The radiometric scan angle correction was not found to be necessary in the low altitude data, because path radiance effects which are the dominant cause of the radiometric scan angle variation are not noticeable at low altitudes. The correction was applied to all but one of the high altitude data sets, where path radiance constitutes a larger portion of the recorded signal.

A geometric scan angle correction is also made during the preprocessing phase to correct for changes in pixel width with scan angle. This correction is made using the altitude, ground speed, and scan rate parameters recorded on the flight data logs. The data is resampled (using nearest-neighbor sampling) onto a regular grid such that the along-scan distance between pixels is the same as the along-path distance. Variations in flight parameters are not accounted for in this correction and may cause geometric distortions in some of the products.

### 3.2 CALIBRATION

The low altitude data sets include lidar measurements of the water depth at regular intervals and at known locations with respect to the passive data. These depth samples are used to "calibrate" the passive data for depth: i.e., to establish a relationship between the passive signals and the water depth. The form of this relationship is

$$z = a + \sum_{i=1}^N b_i \ln(V - V_{s1})$$

where  $a$ ,  $b_1, \dots, b_N$  are the calibration constants and  $v_{si}$  is the deep-water signal in band  $i$ . The data processing described in this report was carried out with  $N = 2$  for all cases.

The high altitude data does not contain such an internal depth calibration source. Three alternative methods of calibration were investigated for the high altitude data. These methods are described in sections 3.2.2 through 3.2.4. Depth charts were prepared using each calibration method, and an analysis of probable errors inherent in each method is presented in section 5.

Bottom feature processing consists of the calculation of the depth-invariant index

$$y = \sum_{i=1}^N c_i \ln(v_i - v_{si})$$

at each point in the scene, where  $c_1 \dots c_N$  are constants related to the water attenuation coefficient [3]. Thus, the calibration phase for bottom feature processing is essentially the determination of the constants  $c_i$ . The  $y$ -value is used to generate a black-and-white continuous tone image in which the film density is related to the bottom reflectance only (i.e., in which the effects of water depth variations have been removed). The calibration procedure for this processing is described in section 3.2.5.

### 3.2.1 LIDAR CALIBRATION

The depth calibration procedure using lidar depth data includes two steps. The first step is the extraction of the lidar depths and the corresponding passive signals from the data tapes. The lidar depths are extracted using a program which locates each lidar data record and plots the amplitude of the pulse versus time on a CRT screen. An operator examines the plot, identifies the surface-reflected and bottom-reflected

pulses, and marks their locations with a cursor. The program then computes the depth based on the time difference between the surface-reflected and bottom-reflected pulses, and writes out this depth as well as the corresponding passive data values into an output file.

The second step is to compute the variables  $x_i = \log(V - V_{si})$  for each data point, where  $V_{si}$  is the deep-water signal for band i, and to execute a regression analysis between the depth (z) and the  $x_i$  values for each possible band pair. This results in a set of equations

$$z = a + b_i x_i + b_j x_j$$

each with an associated correlation coefficient (r). The band pair with the largest correlation coefficient is selected as the optimum band pair for depth processing. The channel numbers and the constants a,  $b_i$ , and  $b_j$  for this band pair are entered into the depth processing program (section 3.3), which then calculates the water depth at each passive data location.

### 3.2.2 TRANSFER OF LIDAR CALIBRATION TO HIGH ALTITUDE DATA

Since the M-8 lidar system cannot be operated at altitudes over approximately 2,000 feet, an alternative method of depth calibration must be used with the high altitude data. One such method is to use the calibration constants obtained from a low altitude pass over the same area, with adjustments for gain and illumination changes. If  $V_{zi}$  is the signal recorded at low altitude in band i over a given location, and  $V_{hi}$  is the signal recorded at high altitude over the same location, the relationship between these signals may be written as

$$V_{hi} = C_i + D_i V_{zi}$$

where  $C_i$  is the difference in path radiance, and  $D_i$  is given by

$$D_i = \frac{T_{hi} E_{hi} G_{hi}}{T_{li} E_{li} G_{li}}$$

where  $T$  is the atmospheric transmittance,  $E$  is the irradiance, and  $G$  is the gain factor. Since the same relationship holds for the deep-water signals, the  $X_i$  variables defined in the previous section are related as follows:

$$X_{hi} = X_{li} + \ln(D_i)$$

Thus, the equation given in the previous section may also be used for calculating the water depth from the high altitude data with the same coefficients  $b_i$  and  $b_j$  and the parameter  $a$  replaced by

$$a' = a - b_i \ln(D_i) - b_j \ln(D_j)$$

Since the parameters  $b_i$  and  $b_j$  are of the same order of magnitude but with opposite sign (c.f., section 4), effects which change  $D_i$  and  $D_j$  in the same direction tend to cancel out. Thus, atmospheric transmittance effects can generally be neglected and irradiance changes can also be ignored if the low and high altitude data are collected in short succession. Gain changes are not necessarily the same in both bands and, therefore, should be taken into account, as should irradiance changes if a long time has elapsed between the low and high altitude runs. The ratio of irradiances may be approximated by the ratio of the cosines of the solar zenith angle: i.e.,

$$\frac{E_{hi}}{E_{li}} = \frac{\cos \theta_h}{\cos \theta_l}$$

where  $\theta_h$  is the solar zenith angle at the time of the high altitude pass and  $\theta_l$  is the solar zenith angle at the time of the low altitude pass.

### 3.2.3. CALIBRATION USING SHIP DATA

The normal procedure for calibration using ship data is to measure the depths, know the locations in a coordinate system, superimpose the coordinate system on the imagery, and then make the connection between pixels, depths, and scanner signals.

The DECCA navigation system was not functioning properly during the part of the bathymetry experiment that we used, therefore, there was no consistent coordinate system upon which to base geographic locations and thus no direct way to make the connection between ship location and pixels on the imagery. Instead aircraft photography was used to supply the link between the location of depth measurements and pixels. Aerial Surveys International Inc., an aerial photography company, was contracted by DMA to photograph the diver sites that were marked by buoys.

Procedurally these buoys were labeled, their location determined in the DECCA system and water depths measured by the ship. A coarse examination revealed that the DECCA locations were consistent within the area of a site. Therefore, depths could be assigned to the pictured buoys. Then if there were geographic features discernable in both the photograph and the imagery, interrelation of pixels and depth measurements was possible.

Three different methods of matching pixels and depths were used. At three sites overlays were made from the photographs that covered buoys.

At two of these sites, North Cat Cay and Bimini there were enough buoys to permit the use of the DECCA coordinates to identify the buoys and determine the ship measured depth at each buoy. Next the geographic

features, both land and underwater, that were common to both the photographs and the imagery were used to match the buoys on the photography to the proper pixels on the imagery.

At the other site, Great Isaac, there was only one buoy in the photography. The coordinate system was established using two points, the buoy and the lighthouse on Great Isaac. Since there was only one buoy, there was only one known depth. To establish more depths the nearby ship transects were put into the coordinate system that was established by the two known points. The transects were used to find broad areas where there was little change in the ship measured depths. Some of these areas were chosen and located on the photography and then the photography matched to the imagery and the appropriate depths assigned to the proper pixel.

The third method was used for the Rocky Heads site. There were no buoys near this site so the ship transects were the only source of depth and location. These transects were used to generate a contour plot of the ocean depth in the Rocky Heads area. A zoom transfer scope was used to match this contour plot to the imagery in the Rocky Heads area. Again broad areas of constant water depth were used to assign depths to the proper pixels.

After depths had been established for all the sites, processing proceeded as described in section 3.2.1 and 3.2.2.

#### 3.2.4 RATIO PROCESSING WITHOUT SURFACE TRUTH

It has been mentioned that the coefficients  $b_i$  and  $b_j$  are of the same order of magnitude and opposite sign. If insufficient data exists to determine these coefficients, a reasonable assumption would seem to be

$$b_i = -b_j = b$$

In fact, this assumption is equivalent to the ratio method described in earlier reports [3,4], in which it is shown that

$$b = \frac{1}{2(K_j - K_i)}$$

and that the water depth calculated using this method is independent of the bottom type as long as the ratio of bottom reflectances in the two bands is the same for all bottom types.

If a reasonable estimate of the water attenuation coefficients  $K_i$  and  $K_j$  can be made, the water depth can be calculated using this method to within an additive constant ( $a$ ). Further, an estimate of this additive constant can be made by requiring that the depth approach a reasonable limit, say 1 meter, at the shoreline. This implies that the constant  $a$  is given by

$$a = 1 - b \ln \left( \frac{V_{oi} - V_{si}}{V_{oj} - V_{sj}} \right)$$

where  $V_{oi}$  and  $V_{oj}$  are the highest signals recorded near the shoreline. In the present study, the values for the water attenuation coefficients were taken from a previous analysis [5] involving M-8 scanner data near North Cat Cay.

### 3.2.5 CALIBRATION FOR BOTTOM FEATURE PROCESSING

For the two-band case, the depth-invariant index described in section 3.2 reduces to

$$y = C_1 X_1 + C_2 X_2$$

where  $c_1 = \frac{k_2}{\sqrt{k_1^2 + k_2^2}} = \frac{k_2/k_1}{\sqrt{1 + (k_2/k_1)^2}}$

and  $c_2 = \frac{-k_1}{\sqrt{k_1^2 + k_2^2}} = \frac{-1}{\sqrt{1 + (k_2/k_1)^2}}$

Thus, the calibration phase consists of the determination of the ratio of attenuation coefficients ( $k_2/k_1$ ) for the wavelength bands used. The wavelength bands used in this study were those determined to be optimum for depth extraction. The ratio of attenuation coefficients is determined from a least-squares fit of the  $X_i$  values over a "training area" having a homogeneous bottom composition [4]. The location of such an area is determined by reference to available aerial photography and by an appraisal of the scatter plot of  $X_1$  versus  $X_2$  (c.f., section 4). The required input parameters could also be obtained by a prior knowledge or estimate of the attenuation coefficients as mentioned in section 3.2.4. However, the ratio of attenuation coefficients ( $k_2/k_1$ ) is more sensitive than the difference ( $k_2 - k_1$ ) to changes in suspended material: therefore, a more precise estimate of the actual attenuation coefficients is required for bottom feature processing than for ratio depth processing.

### 3.3 DEPTH PROCESSING

Once the relationship between the passive signals and the water depth has been determined by the procedures outlined in section 3.2, the actual water depth processing is carried out as described in Reference 1. The depth is calculated for each water pixel for which the signal in both operating bands is greater than  $V_{si} + VD_i$ , where  $VD_i$  is a noise threshold obtained from the deep-water statistics. If the signal in either band is less than this threshold a special data value DEEP1 or DEEP2 is written out. If the signals in both bands are less than the corresponding threshold values, the value DEEP (usually 255) is written out.

Pixels are recognized as being over land if the signal in an infrared band is greater than a threshold value (EDL). The output data value zero is assigned to these pixels.

In order to avoid re-calculation of the depth for a signal pair which has already been encountered, the depths are stored in a two-dimensional array whose indices correspond to the input data values. For each pixel processed, this table is consulted to see if the depth has already been calculated for the pair of data values currently under consideration. If the depth has been calculated, it is read from the table and written out. If not, the depth is calculated and inserted in the table as well as being written into the depth output file.

The depth output file contains an integer data value ranging from 0 to 255 for each pixel, representing the depth in tenths of a meter. In order to display this depth information in chart form, the depths are categorized into 1 meter intervals and a separate color is assigned to each interval. A color image is produced using the ERIM/ERDC Optronics film printer to generate a set of three color separations which are combined photographically to yield the final depth chart.

### 3.4 BOTTOM FEATURE PROCESSING

The bottom feature processing is carried out in a manner similar to the water depth processing. The bottom-type index ( $y$ ) (c.f., Sections 3.2 and 3.2.5) is calculated for all water points having signals larger than the thresholds described in the previous section. Water pixels with lower signals, as well as pixels over land, are assigned special values.

Instead of assigning arbitrary colors to various ranges of the  $y$ -value, however, this variable is allowed to control the film density directly. This results in a continuous tone black-and-white image intended to represent the appearance of the bottom with the effects of attenuation in the overlying water column removed. An example of such a bottom feature map is shown in section 4.

## DATA ANALYSIS AND PROCESSING

The results of the application of the calibration and processing methods described in section 3 to the actual data sets are presented in this section. A few sample products are shown here to illustrate the results, but the actual depth charts and bottom feature maps constitute a separate deliverable item and are not reproduced here.

### 4.1 NORTH CAT CAY (1000 ft)

The preprocessing for the North Cat Cay low altitude data set (Run 3, 8/12/78, 0900) was carried out in two ways in order to illustrate the difference between the two methods. The first method was to perform only a radiometric scan angle correction, as described in section 3.1 and reference 1. The second method was to perform only a sun glint correction, as described in section 3.1.

The first method of preprocessing begins with the calculation of an average deep-water signal as a function of the scan angle. Since Run 3 did not extend over deep water, data from a parallel pass (Run 2) was used for this calculation. Figures 1(a) and 1(b) show the variation of the average deep-water signal in band C8 with scan angle, before and after smoothing. A 50-pixel boxcar smoothing process was applied to obtain the curve shown in Figure 1(b). The steep rise on the left hand side is due to sun glint on the eastern edge of the image. The smoothed data was subtracted pixel-by-pixel from the rest of the data in Run 3 in order to remove the average sun glint signal. This method does not remove the fluctuations in the sun glint signal, so a large "noise" component remains in the sun glint area. Also, if the sun glint pattern changes along the flight path, due to variations in sea state, for instance, the average correction applied by this method will be incorrect.

$\Sigma$ ERIM

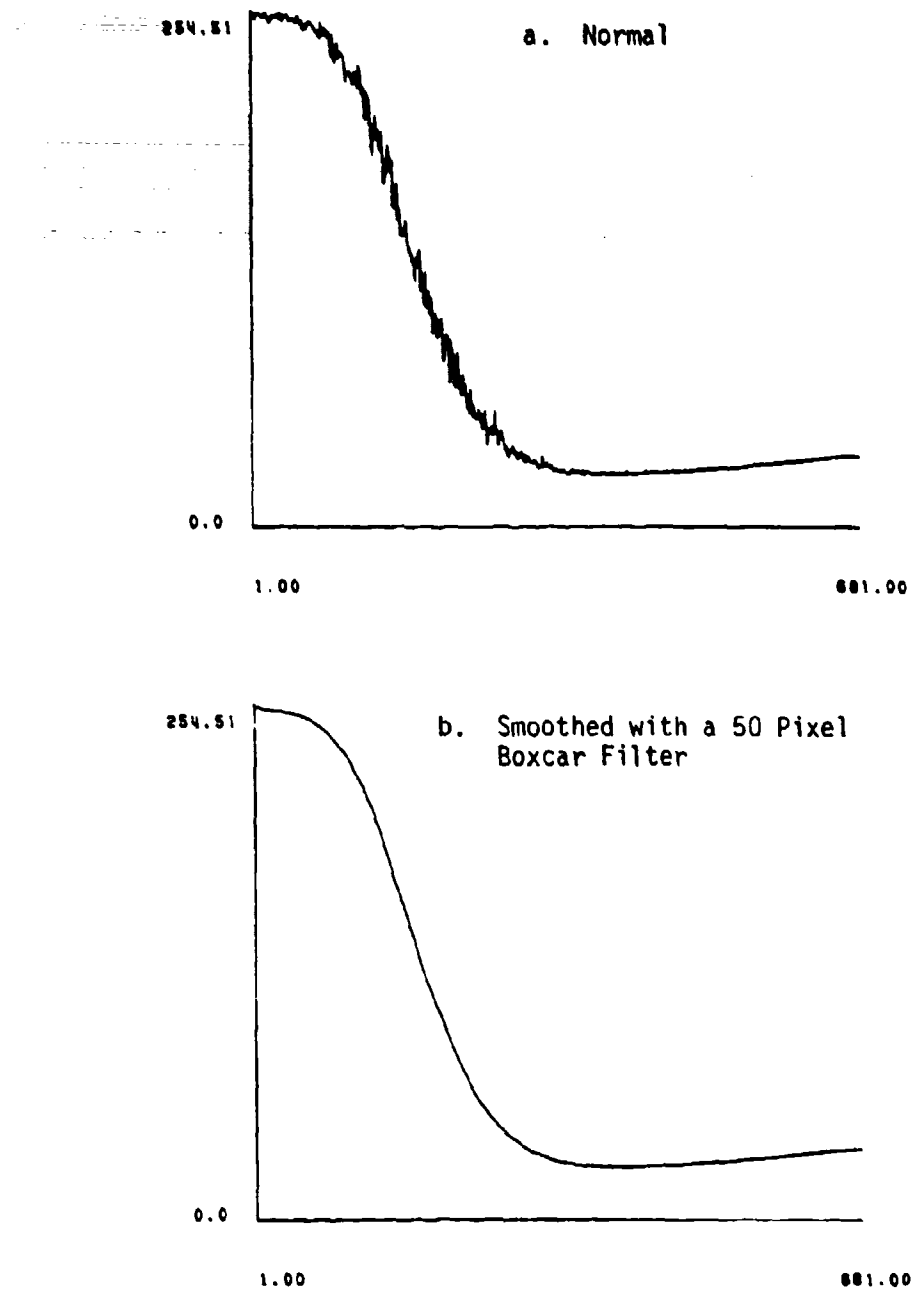


FIGURE 1a and b. AVERAGE DEEP-WATER SIGNAL IN BAND C8 VERSUS  
PIXEL NUMBER. North Cat Cay, Run 2, 8/12/78. 0900.

The second method of preprocessing was initiated by calculating the covariance matrix for the deep water signals in an area of variable sun glint. The signals are chosen over deep water to avoid any influence of shallow water return on the sun glint correction term. Figure 2 shows a scatter plot of the signals in band C8 versus those in band C2. The slope of the regression line for this data is

$$B_{ij} = \frac{\sigma_{ij}}{\sigma_{jj}} = 0.314$$

The correlation coefficient for bands C8 and C2 is 0.957. For bands C5 and C2, the slope is 0.293 and the correlation coefficient is 0.966. Using these coefficients a pixel-by-pixel sun glint correction was applied as described in section 3.1. This procedure results in a reduction in the variance as well as the mean signal over sun glint areas, as shown in Table 2. The corrected signal variance in the sun glint area is still larger than in areas unaffected by sun glint, but a significant improvement is made in the signal-to-noise ratio by this correction.

TABLE 2

COMPARISON OF SIGNAL STATISTICS  
BEFORE AND AFTER SUN GLINT CORRECTION  
(data records 1500-1600, points 250-300)

<u>Before Correction</u>	<u>After Correction</u>
C5:      mean = 35.02 std. dev. = 14.74	mean = 25.26 std. dev. = 4.38
C8:      mean = 84.46 std. dev. = 18.40	mean = 74.01 std. dev. = 10.58

After preprocessing, the depth calibration was carried out using a set of 212 lidar depth samples, as described in section 3.2.1. Figure 3(a) shows a plot of these lidar depths versus the scan line number (all lidar depth measurements are at nadir). The gaps in this plot are due

**ΣERIM**

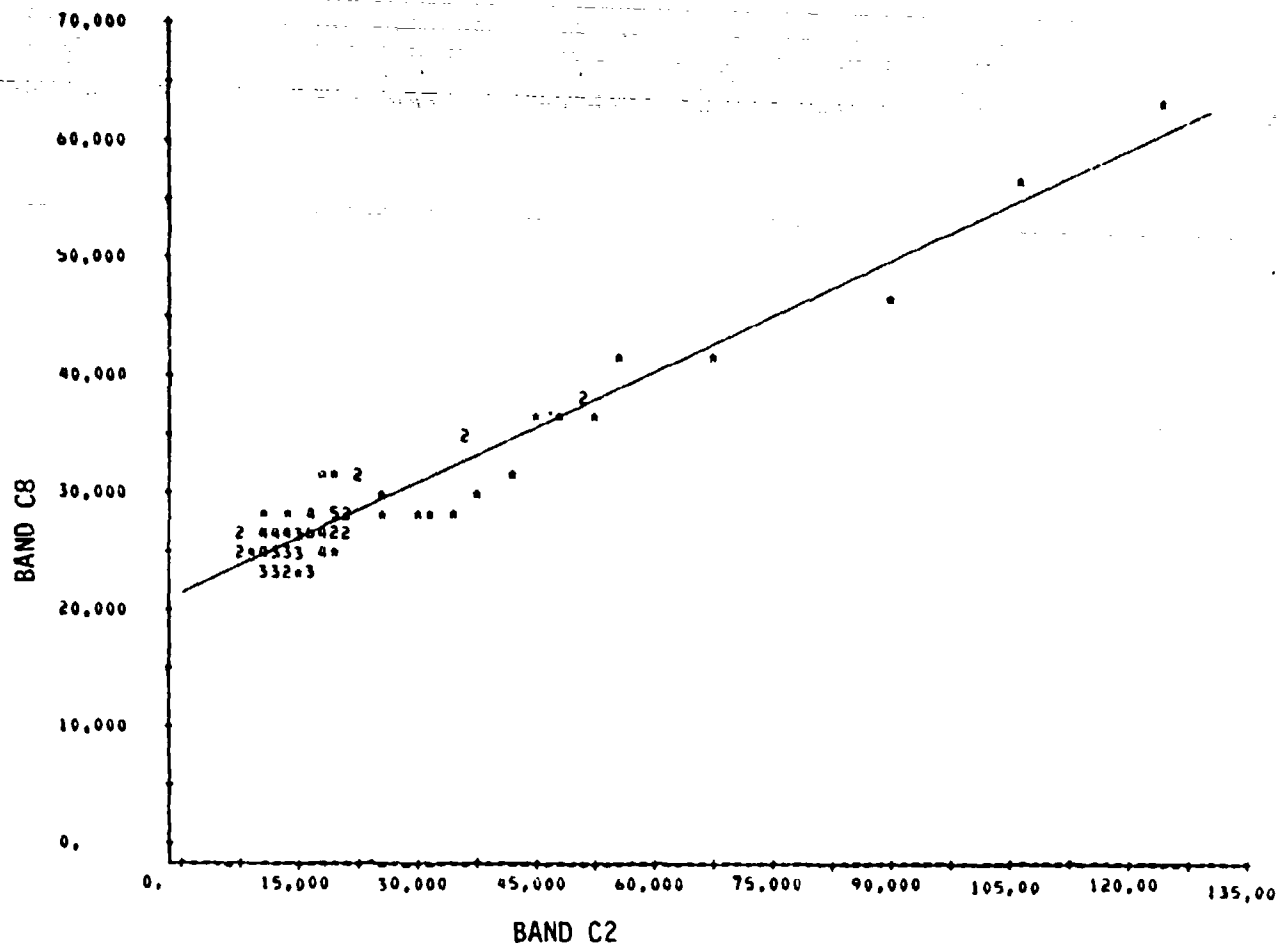


FIGURE 2. SCATTER PLOT OF SUN GLINT SIGNALS IN BANDS C8 AND C2 OVER DEEP WATER (North Cat Cay, Run 2, 8/12/78, 0900). Line indicates least-squares fit to data.

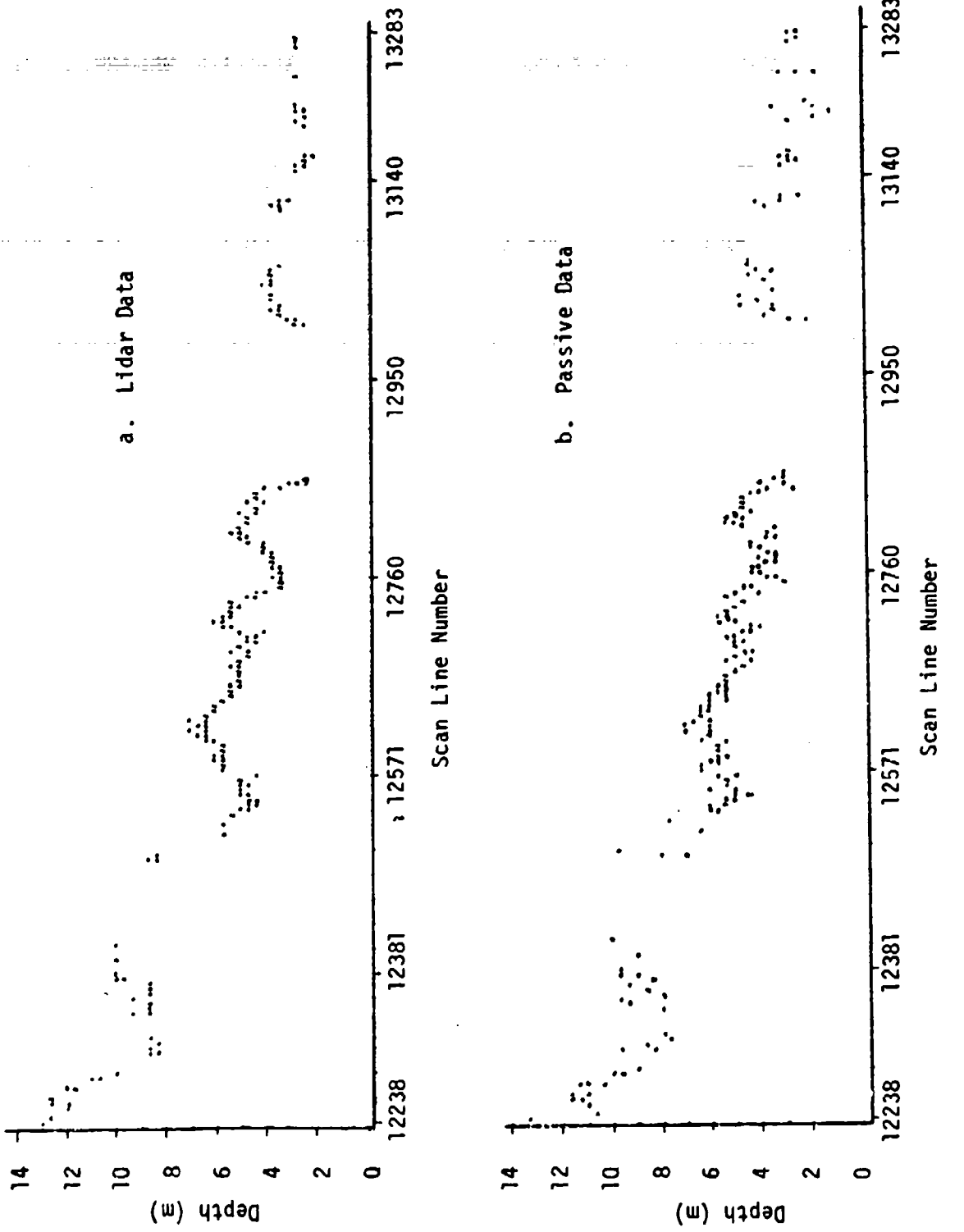


FIGURE 3. COMPARISON OF DEPTHS OBTAINED FROM LIDAR AND PASSIVE DATA FOR NORTH CAT CAY,  
RUN 3, 8/12/78, 0900.

to recording problems which prevented an accurate extraction of the lidar depth for some of the pulses. The gap from scan line number 12855 to 12998 corresponds to the portion of the flight path over North Cat Cay itself.

Depth regressions were run for various band pairs, using data from both preprocessing methods. The optimum band pair was found to consist of bands C5(.58-.64 μm) and C8(.50-.54 μm). For the sun glint corrected data, the depth equation resulting from this analysis is

$$z = 8.477 - 4.883 \ln(V_5 - V_{5S}) + 3.374 \ln(V_8 - V_{8S}).$$

The deep water signals for these bands are  $V_{5S} = 10.65$  and  $V_{8S} = 26.25$ . The correlation coefficient for this band pair is 0.957, and the standard error of the depth estimate is 0.703 meters. The correlation coefficients for several other band pairs is shown in Table 3.

TABLE 3

DEPTH CORRELATION COEFFICIENTS  
FOR VARIOUS BAND PAIRS  
(North Cat Cay, Sun Glint Corrected Data)

<u>Band Pair</u>	<u>Correlation Coefficient(r)</u>	<u>Standard Error (m)</u>
C5/C7	0.949	0.770
C5/C8	0.957	0.703
C5/C9	0.937	0.850
C6/C7	0.730	1.664
C6/C8	0.920	0.956
C6/C9	0.879	1.159

Using the data not corrected for sun glint, the regression analysis yielded the equation

$$z' = 8.627 - 5.033 \ln(V_5 - V_{5S}) + 3.529 \ln(V_8 - V_{8S})$$

with a correlation coefficient of 0.930 and a standard error of 0.897 meters for the depth estimate.

A plot of the depth calculated from the sun glint corrected data versus the scan line number is shown in Figure 3(b). A comparison of the two sets of depths shown in Figure 3(a) and 3(b), and an analysis of the depth errors, is contained in section 5 of this report.

The water depth was calculated for the entire scene using both pre-processing methods, resulting in the depth charts shown in Figure 4. Land was edited out using a threshold of 254 counts in band C2, and appears black in these images. This criterion also resulted in the editing of sun glint areas where the near-infrared band was saturated. The depths shown in the left sides of these images are in quite good agreement, but a large difference appears in the area affected by sun glint. The image which was corrected using the average scanline method exhibits a large amount of apparent depth misclassification on the right side, and also shows evidence of vertical striping, especially in the deeper areas near the bottom of the image. The vertical striping is introduced by the average scan line correction, despite the smoothing described in section 3.1, because of digitization effects. Each time the average scan line changes by one digital count, a visible discontinuity appears in the image. The deep-water threshold was set to zero for these runs, so a depth was calculated for all points with data values greater than the deep-water signal in both bands.

The lidar depth data was also used to calibrate a high altitude data set over this area (c.f., Section 4.5). For the high altitude data, however, band C7 was substituted for band C8 for reasons of data quality. Band C8 was not used because of an excessive amount of saturation or clipping in the areas affected by sun glint, due to the higher gain setting for this band. The depth processing parameters for

**DEPTH CHART FOR THE NORTH CAT CAY AREA**  
**Made From Aircraft Imagery At 1000 ft. Altitude**  
**Calibrated With Laser Depth Data**

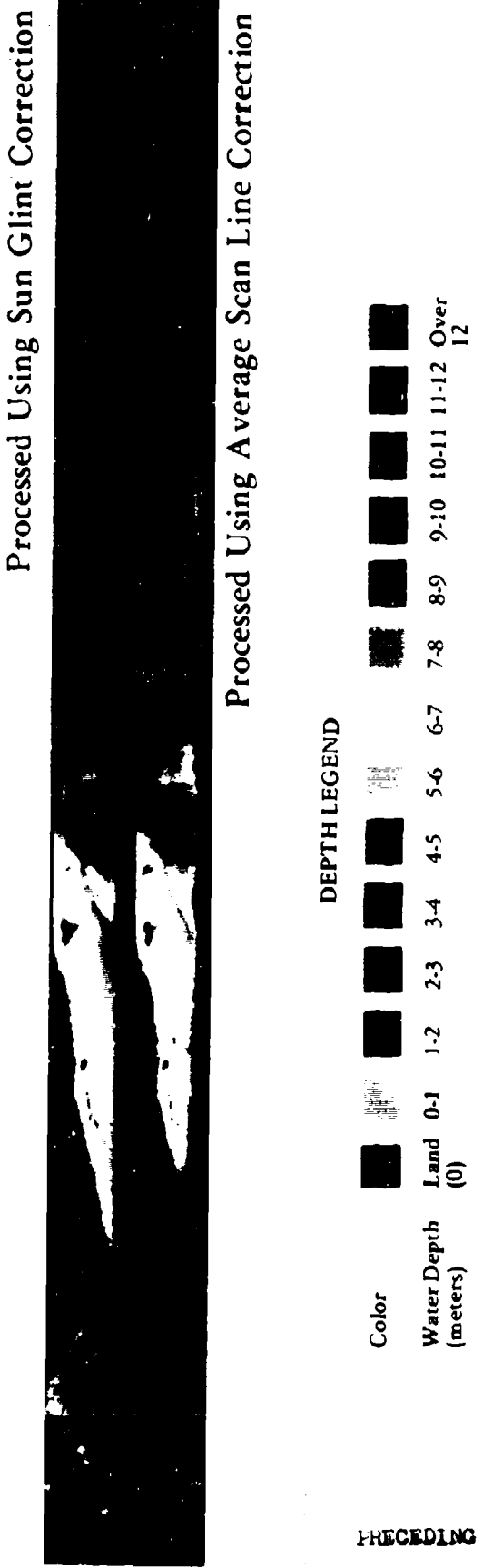


FIGURE 4

PRECEDING PAGE BLANK-NOT FILMED

the C5/C7 band pair, as derived from the lidar data, are therefore also required. These parameters are  $a = 11.423$ ,  $b_5 = -6.369$ , and  $b_7 = 5.463$ . The correlation coefficient for this band pair is 0.949 and the standard error is 0.770 meters, as shown in Table 3.

Bottom feature processing was carried out using the sun glint corrected data for the same bands as used in the depth processing. A scatter plot of  $X_8 = \ln(V_8 - V_{8S})$  versus  $X_5 = \ln(V_5 - V_{5S})$  over a sand area south of North Cat Cay (data records 5200-5300, points 550-680) is shown in Figure 5. The line shown in this figure represents a least-squares fit to the data, as described in section 3.2.5. The slope of this line is

$$\frac{K_8}{K_5} = 0.6332$$

This parameter was used to calculate the bottom-type index ( $y$ ) at each point in the scene. The output of this processing was used to generate the image shown in Figure 6. The dark areas in this image correspond to vegetation beds (mainly Thalassia), as confirmed by field observations [5].

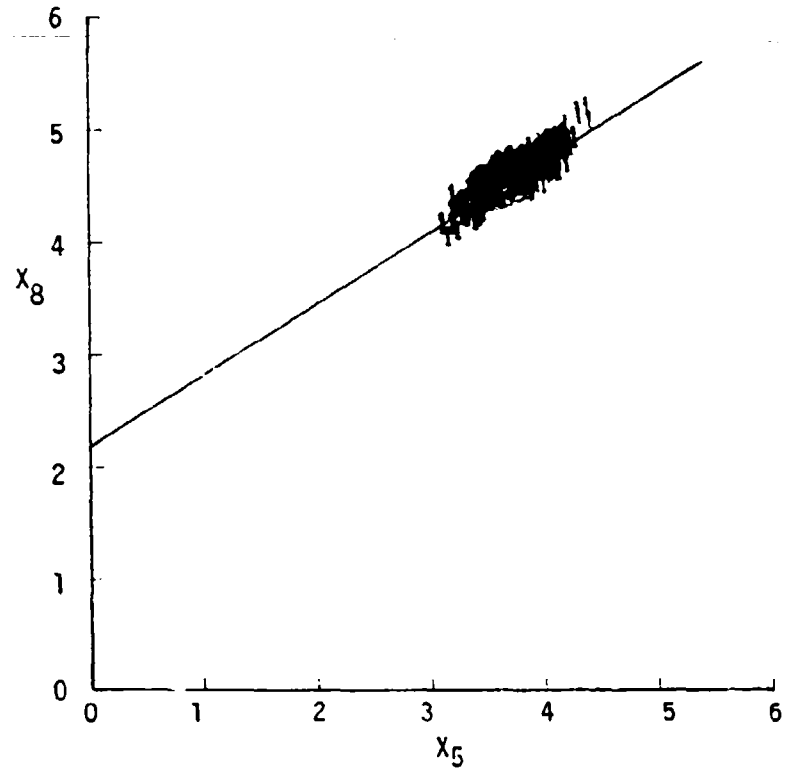


FIGURE 5. SCATTER PLOT OF  $X_8$  VERSUS  $X_5$  OVER SAND BOTTOM NEAR  
NORTH CAT CAY (Run 3, 8/12/78, 0900). Line  
indicates least-squares fit to data.

**BOTTOM REFLECTANCE CHART FOR THE N. CAT CAY AREA**  
**Made From Aircraft Imagery at 1000 ft. Altitude**



FIGURE 6

#### 4.2 BIMINI (1000 ft)

The low-altitude data set over Bimini Island (Run 7, 8/12/78 1600) was processed in a similar manner to the North Cat Cay data set, except that only the sun glint correction preprocessing was done. Deep-water signals were again obtained from a parallel run (Run 4) since Run 7 also did not extend into deep water. These signals were corrected for gain changes using the gain settings recorded on the flight data log.

The sun glint correction coefficients for the operating bands, with C2 as the correction channel, are shown in Table 4. The correlation coefficients for these bands with band C2 were 0.927 and 0.878 respectively.

TABLE 4  
DEPTH PROCESSING PARAMETERS FOR BIMINI  
(1000 FT) DATA SET

	<u>Band C6</u>	<u>Band C9</u>
deep-water signal ( $V_S$ )	17.4	60.0
sun glint correction		
coefficients ( $B_{ijj}$ )	0.855	1.187
depth regression coefficients ( $b_i$ )	-5.326	1.658
(a = 21.122)		

A plot of the lidar depths versus the scan line number is shown in Figure 7(a). Regression of these depths against the passive signals in various band pairs resulted in the selection of bands C6 and C9 as the optimum band pair. The depth processing parameters for this band pair are shown in Table 4. Depth correlation coefficients for this and several other band pairs are shown in Table 5.

$\Sigma$ ERIM

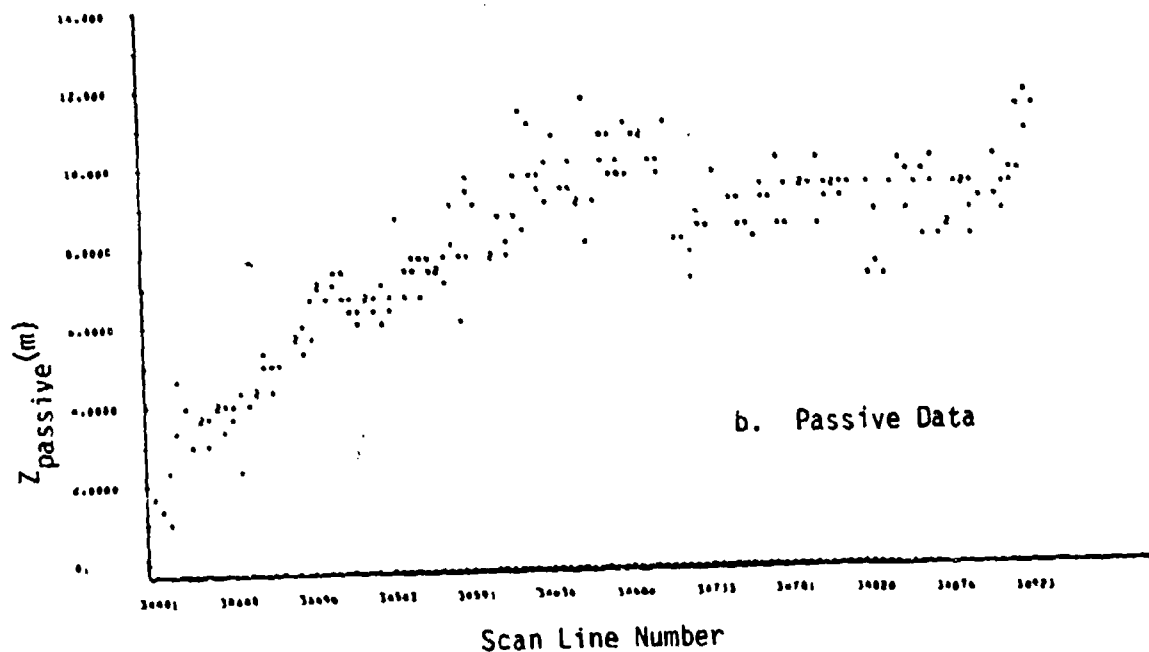
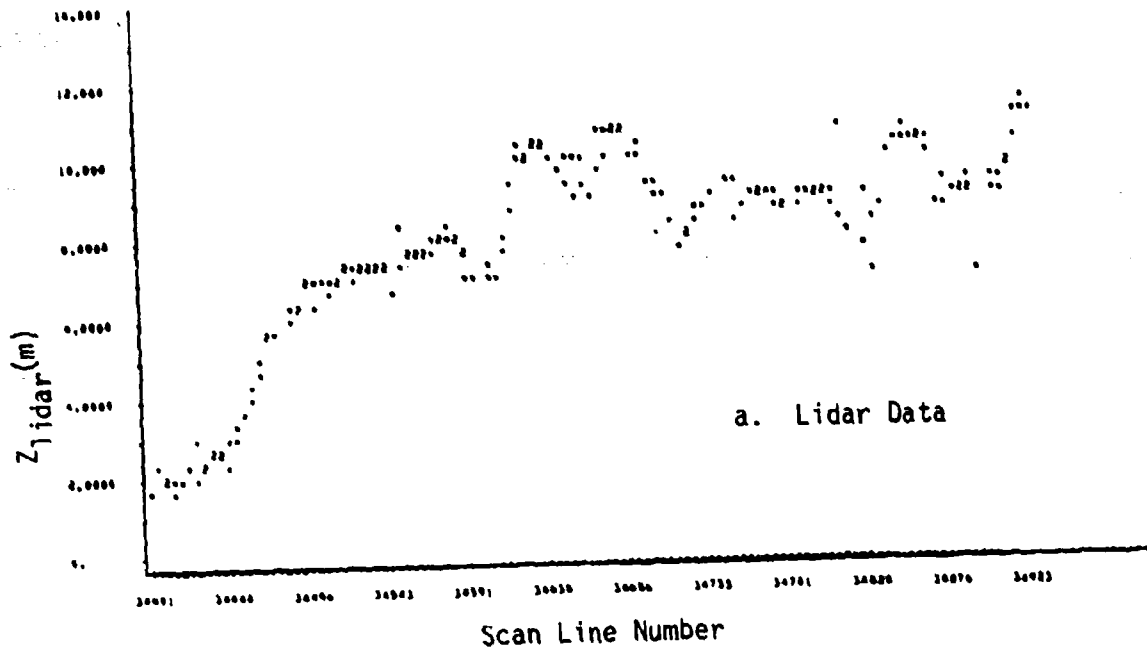


FIGURE 7. COMPARISON OF DEPTHS OBTAINED FROM LIDAR AND PASSIVE DATA FOR BIMINI, RUN 7, 8/12/78 (1600).

TABLE 5

DEPTH CORRELATION COEFFICIENTS FOR VARIOUS BAND PAIRS  
(BIMINI 1000 FT DATA SET)

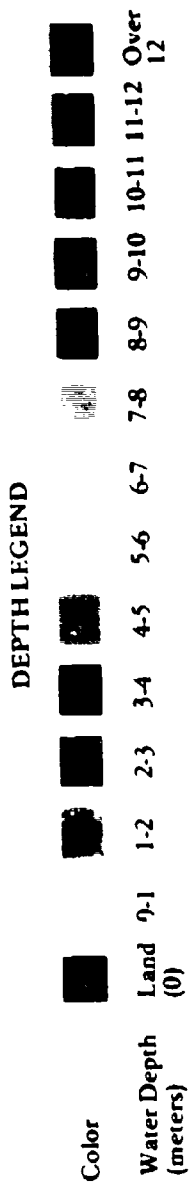
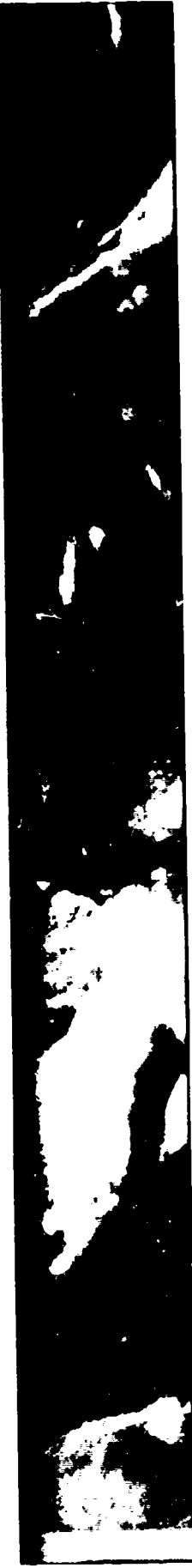
<u>Band Pair</u>	<u>Correlation Coefficient (r)</u>	<u>Standard Error (m)</u>
C5/C7	0.897	1.017
C5/C8	0.904	0.982
C5/C9	0.903	0.988
C6/C7	0.892	1.039
C6/C8	0.915	0.926
C6/C9	0.917	0.914

A plot of the calculated depths at the same locations as the lidar depths is shown in Figure 7(b). An analysis of the depth errors is contained in section 5.

Water depth processing was carried out using the parameters listed in Table 4. The deep-water threshold VD was set to zero, as in the North Cat Cay data set, in order to calculate depths for all pixels with data values greater than the deep-water signal. Band C2 was again used for land editing, with a threshold of 150 counts. A color-coded depth chart was produced for this data set and is shown in Figure 8.

Calibration for bottom feature processing was accomplished by "training" on an area near Moselle bank (data records 5100-5500, points 1-250). A scatter plot of the X-values for bands C9 versus band C6 is shown in Figure 9. The line representing a least-squares fit to this data has a slope of 0.7062. This value was used for processing the data set and generating a black-and-white bottom feature map which is shown in Figure 10.

DEPTH CHART FOR THE BIMINI AREA  
Made From Aircraft Imagery At 1000 ft. Altitude  
Calibrated With Laser Depth Data



PRECEDING PAGE BLANK-NOT FILLED

FIGURE 8

$\Sigma$ ERIM

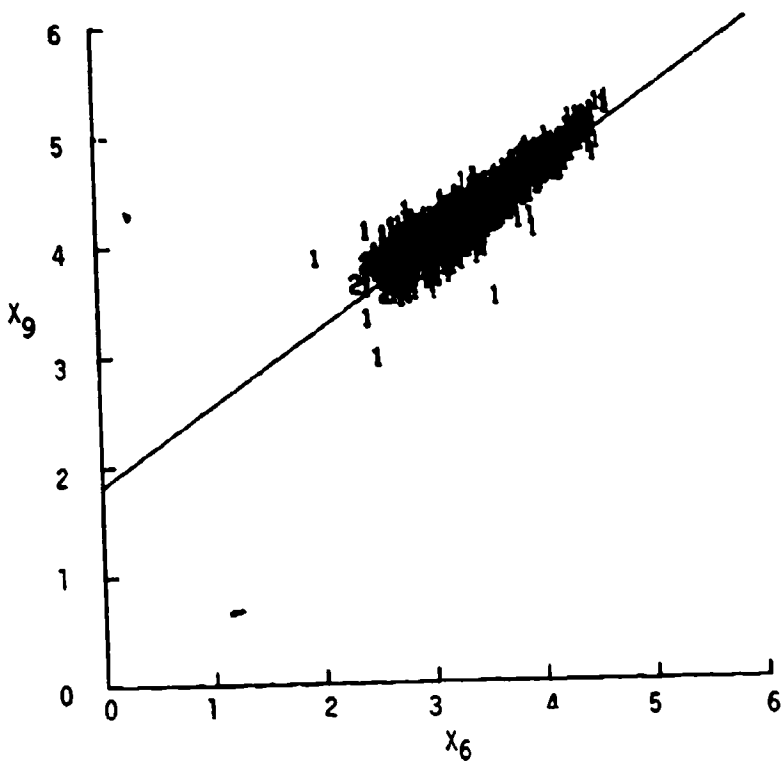


FIGURE 9. SCATTER PLOT OF  $x_9$  VERSUS  $x_6$  OVER SAND BOTTOM NEAR MOSELLE BANK, OFF BIMINI (RUN 7, 8/12/78, 1600). Line indicates least-squares fit to data.

**BOTTOM REFLECTANCE CHART FOR THE BIMINI AREA**

Made From Aircraft Imagery at 1000 ft. Altitude

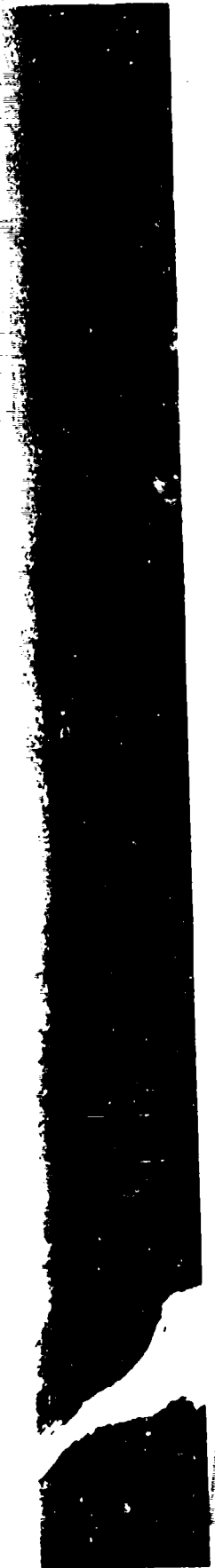


FIGURE 10

PRECEDING PAGE BLANK-NOT FILMED

#### 4.3 GREAT ISAAC ISLAND (1000 ft)

A third low altitude data set near Great Isaac Island (Run 2, 8/12/78, 1600) was selected for analysis in order to determine a set of depth processing parameters to be transferred to the high altitude pass over the same area (c.f. section 4.7). Because of the rapid increase in depth away from Great Isaac Island, and a recording problem which obscured most of the pulses at depths over 8 meters, only 14 lidar depths were available for this run.

A sun glint correction was applied to the data, and a series of regression analyses were run for the water depth against the same set of band pairs as considered in the previous data sets. A second complicating factor was the fact that the passive data in band C6 was saturated in 8 out of 14 cases. Thus the regressions involving C6 have a much lower correlation coefficient and a higher standard error than those involving C5, as shown in Table 6. Unfortunately, data quality constraints, i.e., signal-to-noise ratio, dictated the use of bands C6 and C8 in the high altitude data set (c.f., section 4.7).

For the optimum band pair (C5/C8) the depth regression equation is

$$z = 15.575 - 4.617 \ln(V_5 - V_{5S}) + 2.530 \ln(V_8 - V_{8S})$$

TABLE 6

DEPTH CORRELATION COEFFICIENTS FOR VARIOUS PAIRS  
(Great Isaac 1000 ft Data Set)

<u>Band Pair</u>	<u>Correlation Coefficient (r)</u>	<u>Standard Error (m)</u>
C5/C7	0.865	0.615
C5/C8	0.933	0.442
C5/C9	0.854	0.730
C6/C7	0.557	1.018
C6/C8	0.530	1.039
C6/C9	0.546	1.027

For the band pair used in processing the high altitude data set (C6/C8) the depth regression equation is

$$z = 10.783 - 1.801 \ln(V_6 - V_{6S}) + 0.921 \ln(V_8 - V_{8S})$$

Since the purpose of this analysis was to provide depth calibration information for the high altitude data set, no actual depth processing was done and no images were produced for the low altitude data. The high altitude depth chart and bottom reflectance are shown in Figures 20 and 21, respectively in section 4.7.

#### 4.4 GRAND BAHAMA ISLAND

Two sets of imagery of the southern coast of Grand Bahama Island show unusual patterns in the wavelength region (8-14  $\mu\text{m}$ ) (Figure 11). These patterns occur in shallow water regions along the shoreline. The bottom is sandy with a sharp transition to a vegetated area not far from the shore.

One reaction to the observation of these patterns was that perhaps in some special instances there may be a relationship between water depth and signal changes in the thermal infrared spectral region.

To test this observation, a procedure was established to extract the depths from the lidar data, determine the correlation with depth as seen in the visible (red and/or green) imagery, and finally to find the degree of correlation, if any, between depth and the surface thermal patterns.

The lidar data for these runs was very noisy, causing concern about the reliability of the extracted depths. In an effort to establish confidence in these measured depths, calculations were made using visible data from the same runs. Band C5 and C8 (see Table 1) were chosen for the calculations since they have been shown to be good indicators of depth. An estimate of the deep water signals in these visible bands was made and the equation that was developed for North Cat Cay was used to make the calculations. The idea here was to get an indication of the magnitude of the depths to check the reliability of depths observed with the lidar. Figure 12 shows a plot of these calculated depths versus the measured depths. It can be seen that there is not enough difference between the calculated and measured depths to cause concern about the reliability of the measurements. This calculation also adds confidence for the correlations to be made between the depths extracted from the visible spectral channels and the possibility of the thermal surface patterns being used as depth indicators.

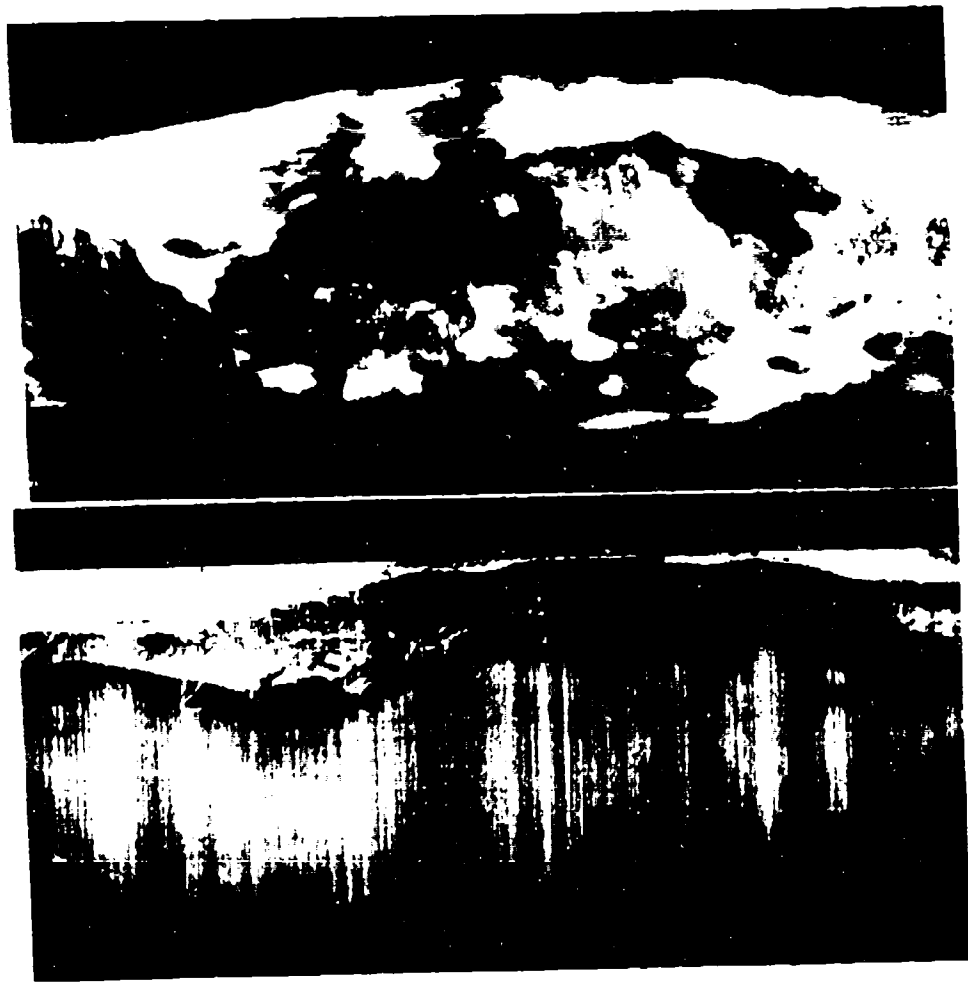
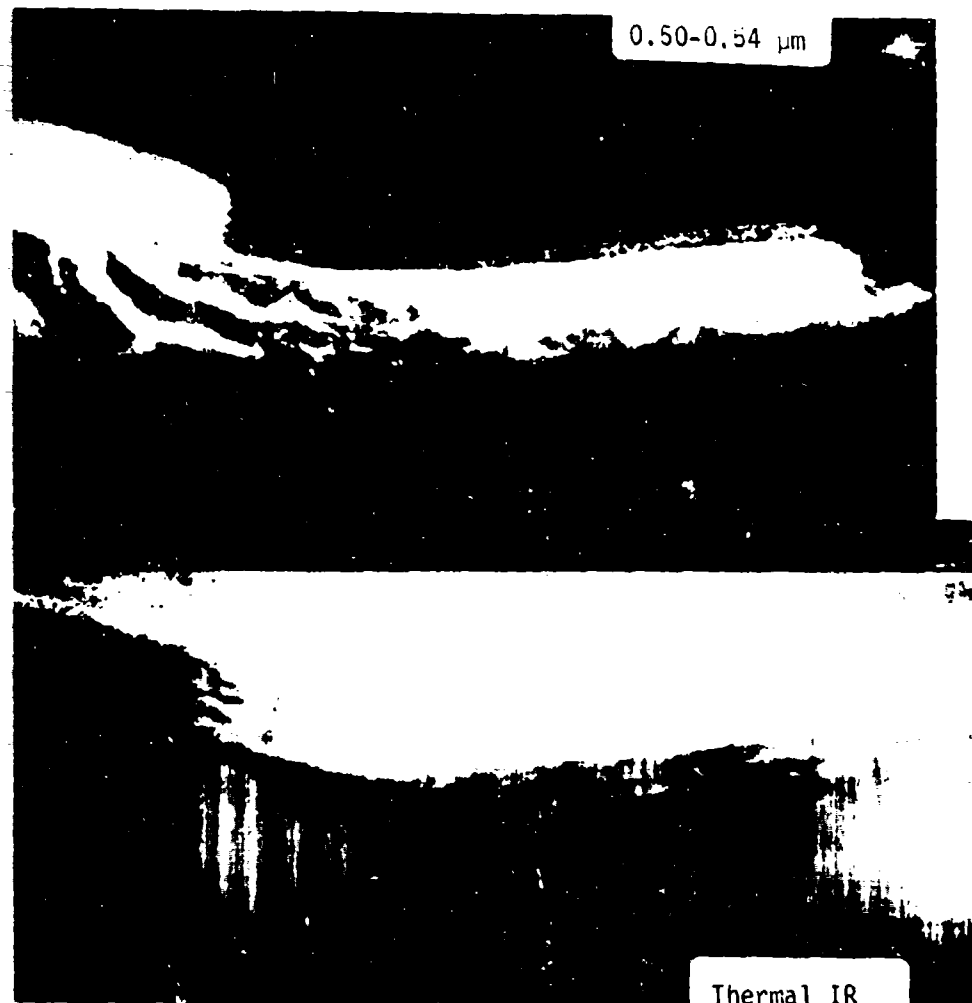


FIGURE 11. IMAGERY OF GRAND BAHAMA ISLAND, RUN 1, 8/13/78, 0900

LEFT HALF

0.50-0.54  $\mu$ m



Thermal IR

RIGHT HALF

**ΣERIM**

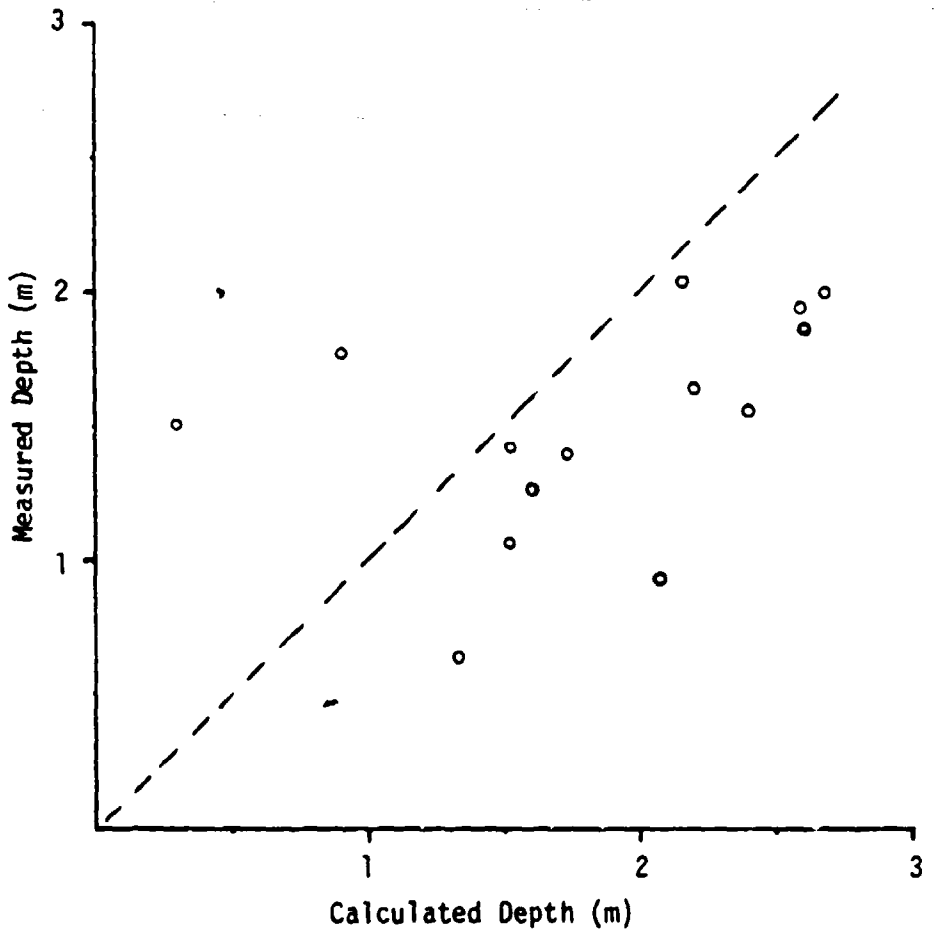


FIGURE 12. MEASURED DEPTH VERSUS CALCULATED DEPTH, GRAND BAHAMA ISLAND (RUN 1, 8/13/78, 0900)

A plot was made of  $\ln(V_5 - V_{5s})$  versus depth (Figure 13),  $\ln(V_8 - V_{8s})$  versus depth (Figure 14), and  $\ln A_1$  versus depth (Figure 15). ( $A_1$  is the 8-14  $\mu\text{m}$  thermal band.) From these figures it can be seen that both the  $V_5$  and  $V_8$  plots show some depth dependence, but there does not appear to be any depth related effect in the  $A_1$  plot. Depth samples were taken along the nadir track, over a range of depths from 0.45 m to 2.05 m.

Least squares regressions were made for each of these three channels against depth and the correlation coefficients were:

C5 and Depth .4267

C8 and Depth .3606

A1 and Depth .0048

Both the coefficients for C5 and C8 indicate that some of the variance in depth is "explained" by variations in the signals, , while the coefficient for channel A1 implies that none of the "variance" is explained.

The channels, C5 and C8 have proved useful as depth indicators in the past and have correlation coefficients that are in the range expected, to show depth dependence, while the coefficient for channel A1 indicates that this channel did not respond to depth changes for this site. While this local observation did not show correlation, the shallow water of the entire Great Bahama Bank has been observed distinctly on Nimbus 7 thermal imagery despite the fact that the measurements of the absorption properties of water indicate that in the thermal wavelength region a sensor may penetrate to about 3 mm. Any changes that are observed in the A1 signals must be caused by temperature changes of the water surface, or changes in the emitting properties of the surface.

There are other possible explanations for the unusual patterns in the thermal imagery that can best be explained by observations made at the surface at the same time that the imagery is taken. Among the explanations are the differential heating of the water column because of bottom reflectance differences, discharge of underground freshwater

**ERIM**

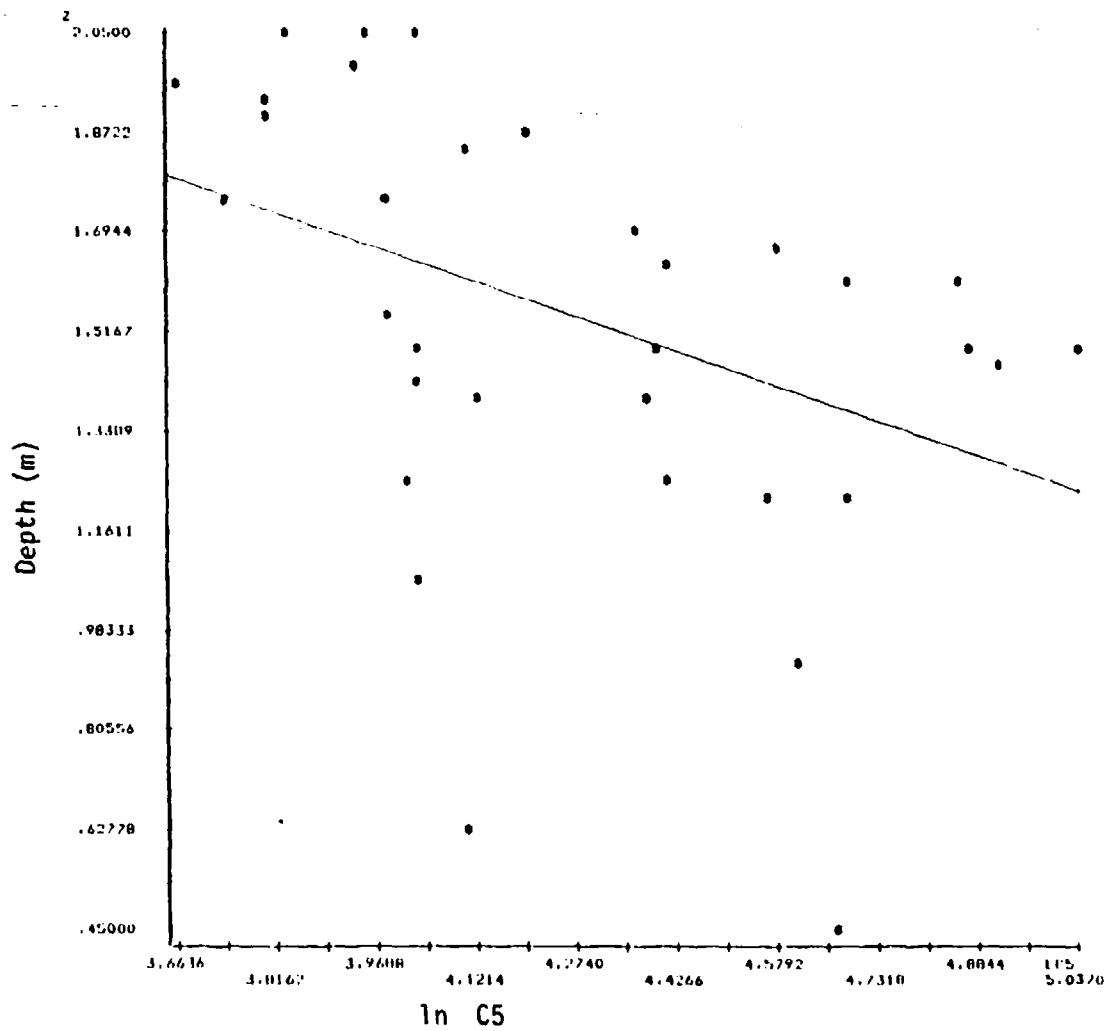


FIGURE 13. DEPTH VERSUS SIGNAL FOR BAND C5

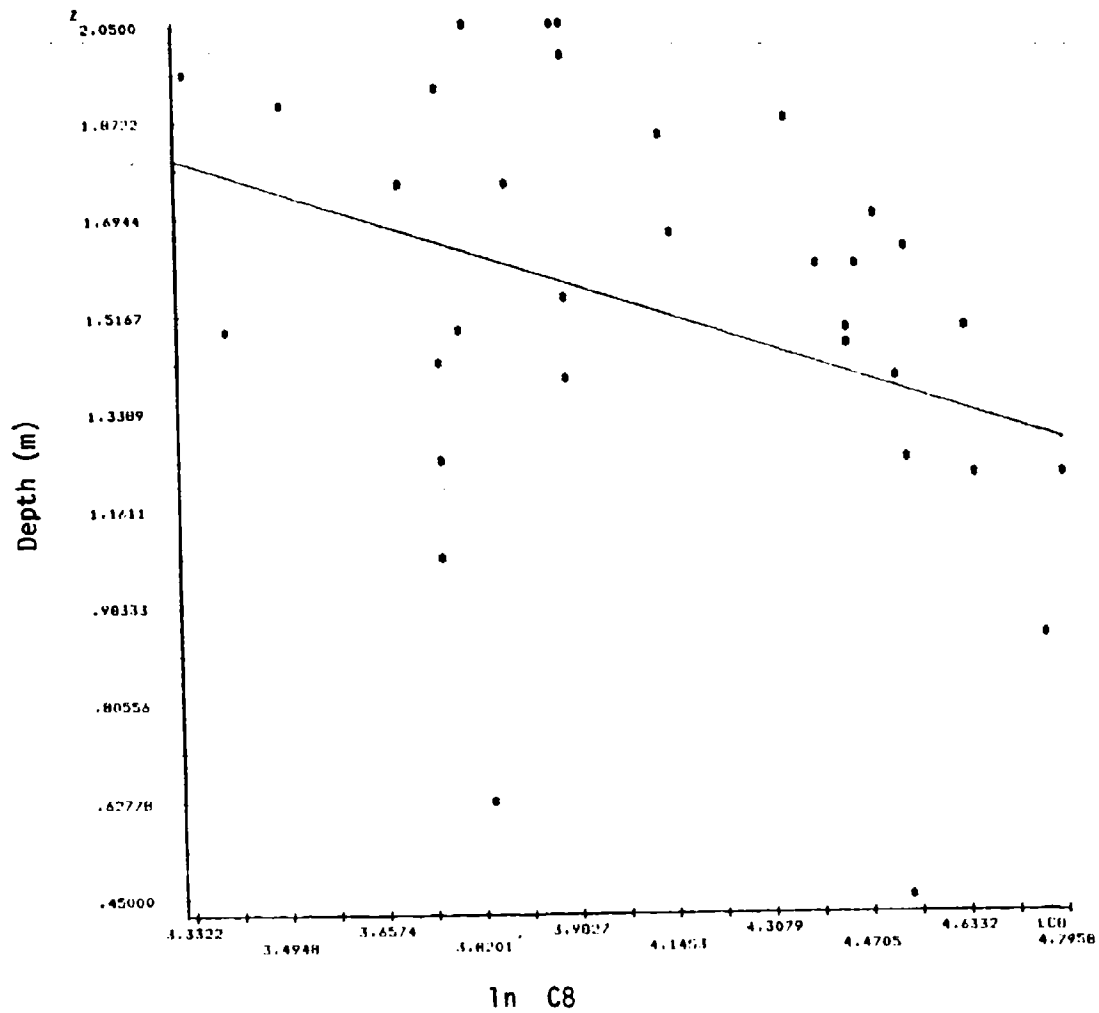


FIGURE 14. DEPTH VERSUS SIGNAL FOR BAND C8

$\Sigma$ ERIM

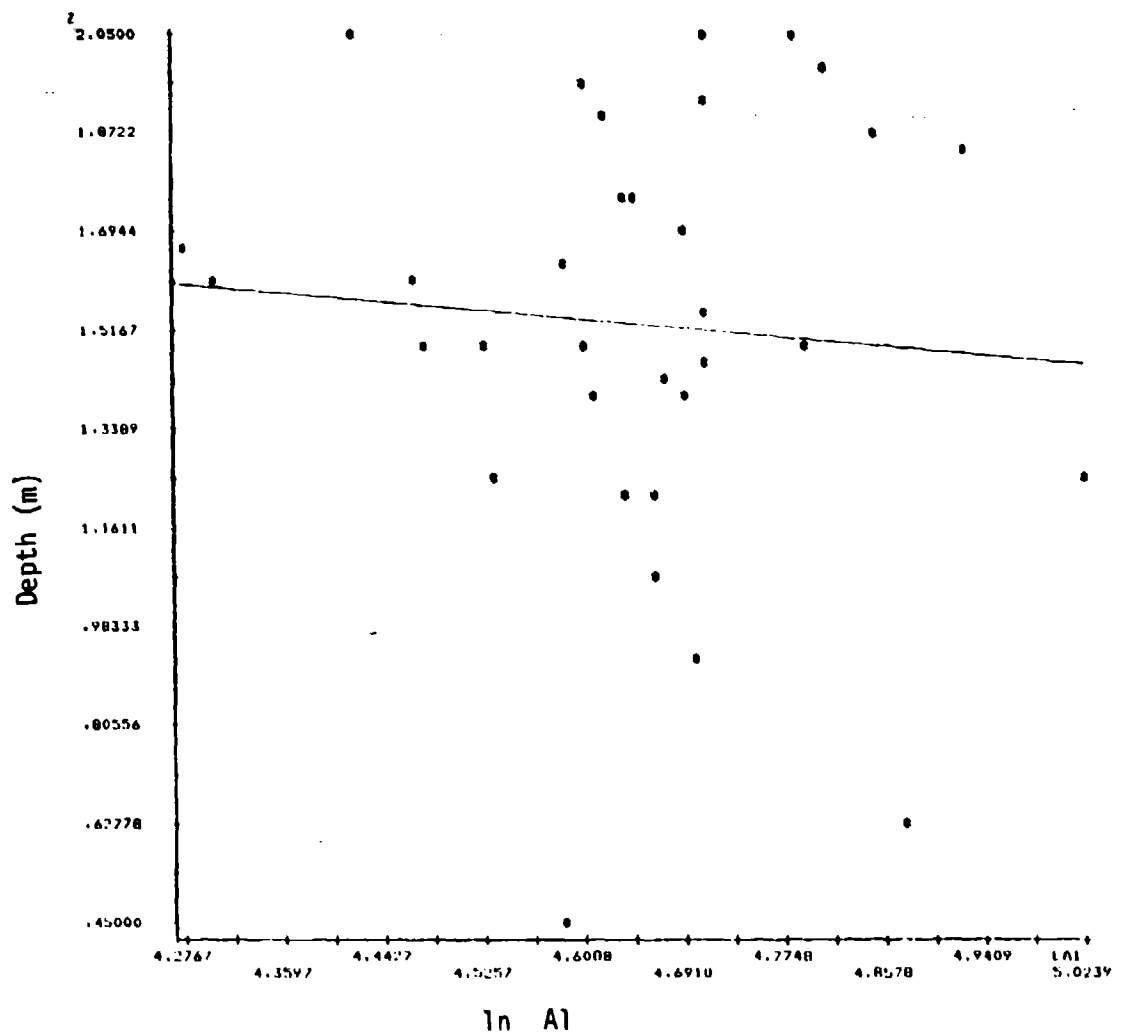


FIGURE 15. DEPTH VERSUS SIGNAL FOR BAND A1

along the shoreline, that reaches the surface because of the different density of the ocean water or the mixing of backwash water warmed by the beach with the cooler oncoming ocean waves. Not all thermal surface patterns can be interpreted as depth related but the special cases, where the detection of submerged reefs and shoals by differential heating of the water column is possible, need to be documented.

#### 4.5 NORTH CAT CAY (10,800' RUN)

The high altitude data set for North Cat Cay required preprocessing to correct for both sunglint and scan angle effects. Band C2 was used for calculating the sunglint correction coefficients. The correlation coefficients for C2 with the operating bands (C5 and C7) are 0.966 and 0.960. The correction coefficients ( $B_{ij}$ ) are 0.290 for C5 and 0.234 for C7. (These are calculated as described in section 3.1, using the parameters listed in Table 9.) The reduction in sunglint is illustrated in Table 7.

TABLE 7

COMPARISON OF SIGNAL STATISTICS  
BEFORE AND AFTER SUNGLINT CORRECTION  
(data records 700-800, points 280-400)

<u>Before Correction</u>	<u>After Correction</u>
C5: mean = 53.55 std. dev. = 13.96	mean = 39.92 std. dev. = 3.51
C7: mean = 52.74 std. dev. = 11.29	mean = 41.75 std. dev. = 3.04

The infrared channel (C2) was saturated in the left side of the swath (pixels 1-230). Since a sunglint correction was not possible for these points, the first 230 pixels were excluded from the processing of this data set. Band C2 was also used for land editing, with a threshold of 250 counts used for defining the land/water boundary.

The average scan line across deep water was calculated from data records 2-300. It was smoothed with the 50 pixel boxcar process and subtracted from the rest of the data set, to offset scan angle variations. The average corrected deep water signal ( $V_S$ ) was 39.98 for C5 and 42.29 for C7. The deep water threshold ( $V_D$ ) was set to 5, so any pixel with a signal less than 5 counts above  $V_S$  was labeled DEEP.

Three methods of depth calibration were used for processing the high altitude data, as described in section 3.2. The lidar depth processing parameters for the high altitude pass were developed from the calibration of the low altitude pass over the same area (c.f., section 4.1). The coefficients were adjusted for the difference in gain settings and applied to the high altitude data. The gain setting for C7 was 2 for the low altitude pass, and 5 for the high altitude pass, but remained constant for C5. Therefore for band C7,  $V_h = 5/2V_L$ , and  $\ln(V_L) = -0.916 + \ln V_h$ . The revised lidar depth regression equation is:

$$z = 6.417 - 6.369 \ln(\Delta V_{5h}) + 5.463 \ln(\Delta V_{7h}).$$

The ship data calibration was calculated from water depths measured at six buoys (Table 8). The buoys were located on the high altitude image and the average signals in Bands C5 and C7 for the surrounding 3 x 3 pixels were extracted. The logs of the signals in both bands were regressed against the measured depths with a correlation of 0.987 and standard error of 0.968 meters. The depth processing coefficients, obtained from this regression are:  $a = 4.370$ ,  $b_1 = -8.206$ ,  $7.471$ .

TABLE 8

NORTH CAT CAY (10,800' RUN)  
SHIP BUOY LOCATIONS

Z	UTM-N	UTM-E	LINE	POINT	$\ln(V-V_S)$ C5H	$\ln(V-V_S)$ C7L
3.8 m	2826434	672865	2124	312	3.549	3.727
3.4 m	2825825	673611	2122	282	4.392	4.563
6.8 m	2825793	672719	2008	333	3.423	4.852
12.3 m	2825503	672471	1966	356	2.699	4.363
13.7 m	2826086	671944	2068	402	2.062	3.915
13.1 m	282600	671883	2056	409	1.768	3.218

The third type of depth processing used the ratio method described in section 3.2.4. The water attenuation coefficients ( $k$ ) for bands C5 and C7 were assumed to be  $0.203\text{m}^{-1}$  and  $0.114\text{m}^{-1}$ , respectively [5]. The multiplicative coefficients in the depth equation are therefore (c.f. section 3.2.4)  $b = 1/2\Delta k = 5.62\text{m}^{-1}$ . The brightest water pixel was identified near the southwest shore of North Cat Cay (data record 2191, point 326), so that at an assumed depth of 1 meter,  $V_5 = 242$  and  $V_7 = 197$ . Therefore, the additive coefficient in the depth equation is:

$$a = 1 + 5.62 \ln(\Delta V_5 / \Delta V_7) = 2.50.$$

The processing parameters for the high altitude passes are summarized in Table 9. Depth charts and bottom feature maps for the North Cat Cay area are shown in Figures 16 and 17, respectively.

TABLE 9  
PROCESSING PARAMETERS FOR HIGH ALTITUDE PASSES

Data Set:	North Cat Cay (10,800' Run)	Bimini (10,800'Run)	Great Isaac (10,800'Run)	Rocky Heads (10,800'Run)
Operating Bands (1)	C5	C6	C6	C6
(2)	C7	C9	C8	C8
Sunglint Correction Parameters				
$\sigma_{1j}$	625.231	1176.891		2249.754
$\sigma_{2j}$	502.945	1685.297		1139.062
$\sigma_{jj}$	2153.066	3633.824		2840.027
$B_{ij}(1)$	.290	.464		.792
$B_{ij}(2)$	.234	.324		.401
Avg. Deep Water Signals				
$V_S(1)$	39.98	17.95	113.98	91.99
$V_S(2)$	42.29	23.44	98.83	67.3
Lidar Depth Processing Coefficients				
a	6.417	18.83	10.783	
$b_1$	- 6.369	- 5.326	- 1.801	
$b_2$	5.463	1.658	.921	
Ship Data Depth Processing Coefficients				
a	4.370	40.201	20.681	
$b_1$	- 8.206	- 15.421	- 4.822	
$b_2$	7.471	5.782	1.225	
"No Surface Truth" Depth Processing Coefficients				
a	2.50	12.199	16.809	
$b_1$	- 5.62	- 9.434	- 13.16	
$b_2$	+ 5.62	+ 9.434	+ 13.16	

**DEPTH CHART FOR THE N. CAT CAY AREA**  
**Made From Aircraft Imagery At 10,800 ft. Altitude**

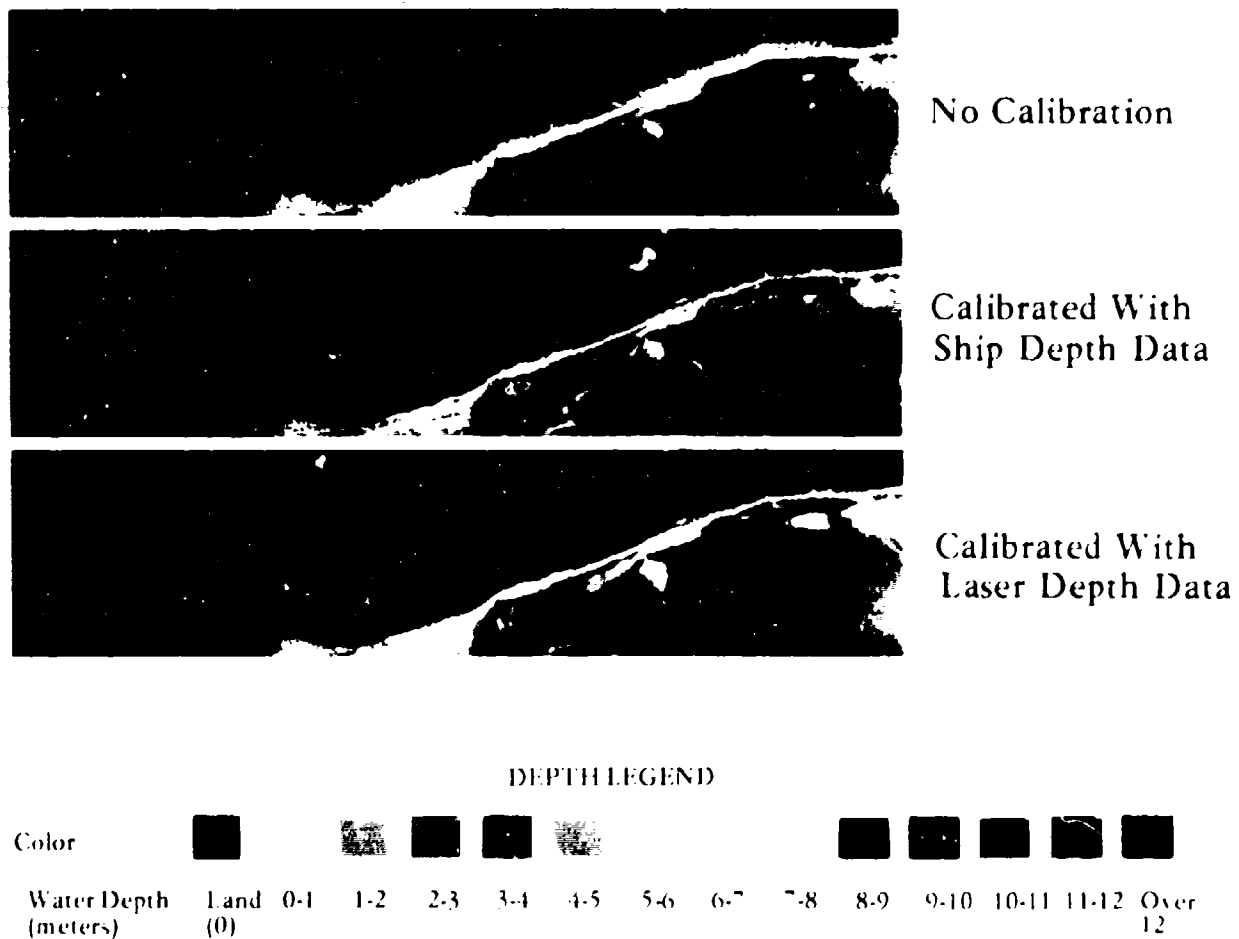


FIGURE 16

**BOTTOM REFLECTANCE CHART FOR THE N. CAT CAY AREA**  
**Made From Aircraft Imagery at 10,800 ft. Altitude**



**FIGURE 17**

#### 4.6 BIMINI (10,800' RUN)

For the Bimini data set (Run 7, 8/12/78, 0900) only the sunglint preprocessing was carried out, since the scan angle variations after the glint correction were minimal. Statistics calculated over a deep water area with variable sunglint established the correlation between Band C2 and Bands C6 and C9 to be 0.993 and 0.977, respectively. The sunglint correction coefficients for the same two bands are 0.464 for C6 and 0.324 for C9. The reduction in the sunglint effects is illustrated in Table 10.

TABLE 10

COMPARISON OF SIGNAL STATISTICS  
BEFORE AND AFTER SUNGLINT CORRECTION  
(data records 2-100, points 150-350)

<u>Before Correction</u>	<u>After Correction</u>
C6: mean = 87.94 std. dev. = 28.16	mean = 16.00 std. dev. = 3.05
C9: mean = 72.25 std. dev. = 19.99	mean = 22.02 std. dev. = 4.12

The average corrected deep water signal ( $V_S$ ) is 17.95 for C6 and 23.44 for C9.

The Bimini depth processing was similar to the other high altitude passes. For this data, the land edit threshold (EDL) in C2 was 254 counts and the deep water threshold ( $V_D$ ) was set to 3.

The lidar depth calibration for the low altitude Bimini data (c.f. section 4.2) was adjusted to fit the high altitude data. To correct for

a large difference in solar elevation at time of overpass, an irradiance ratio was calculated. For bands C6 and C9, this ratio was

$$\frac{\sin 30^\circ}{\sin 78^\circ} = 0.511.$$

The gain ratios for the same operating bands are 5 and 10, respectively. Therefore, the relationship between low and high altitude signals is  $V_{6L} = 2.555V_{6H}$  and  $V_{9L} = 5.112V_{9H}$ . The depth coefficients ( $b_i$ ) remained the same as for the low altitude data. The revised additive coefficient is

$$a = 21.122 - 0.5326 \ln(2.556) + 1.658 \ln(5.112) = 18.3.$$

The ship data depth parameters were calculated from the average signal (V) at seven buoys identified in the Bimini data (Table 11). For the regression of measured depths against  $\ln(\Delta V_6)$  and  $\ln(\Delta V_9)$  at each location, the correlation coefficient was 0.985 with a standard error of 0.363 meters. The resultant depth coefficients are:  $a = 40.201$  and  $b_i = -15.421, 5.784$ .

TABLE 11

- BIMINI (10,800' RUN)  
SHIP BUOY LOCATIONS

Z	N	E	LINE	POINT	$\ln(V-V_S)$	$\ln(V-V_S)$
					C6	C9
9.00 m	2854154	673525	2762	287	3.1566	2.9847
5.82 m	2854028	673783	2734	357	3.3918	3.0860
10.39 m	2854170	673241	2746	411	2.9760	2.8202
9.74 m	2854282	673753	2810	376	3.1281	3.0657
6.47 m	2854720	673281	2888	402	3.3652	3.2367
8.82 m	2854698	673888	2920	389	3.2895	3.3003
7.46 m	2854657	673363	2892	399	3.2768	3.0393

To establish the third set of depth parameters, the high altitude data off the north shore of Bimini Island was examined. The brightest pixel (data record 2680, point 170) was identified, and assumed to represent a depth of 1 meter. The signals at this location are 146 counts in band C6, and 80 counts in band C9. Previously determined attenuation coefficients ( $K$ ) for the same two bands are  $0.146\text{m}^{-1}$  and  $0.093\text{m}^{-1}$ , so the multiplicative coefficients are  $b_1 = 1/2\Delta K = \pm 9.434$ . The additive coefficient ( $a$ ) is:

$$a = 1 + 9.434[\ln(\Delta V_6) - \ln(\Delta V_9)] = 12.199.$$

The depth charts and bottom reflectance image are shown in Figures 18 and 19, respectively.

DEPTH CHART FOR THE BIMINI AREA  
Made From Aircraft Imagery At 10,800 ft. Altitude



No Calibration



Calibrated With  
Ship Depth Data



Calibrated With  
Laser Depth Data

DEPTH LEGEND

Color



Water Depth  
(meters)

Land  
(0)

0-1

1-2

2-3

3-4

4-5

5-6

6-7

7-8

8-9

9-10

10-11

11-12

Over  
12

FIGURE 18

**BOTTOM REFLECTANCE CHART FOR THE BIMINI AREA**

**Made From Aircraft Imagery at 10,800 ft. Altitude**



**FIGURE 19**

**PRECEDING PAGE BLANK-NOT FILMED**

#### 4.7 GREAT ISAAC AND ROCKY HEADS (10,800' RUNS)

The Great Isaac and Rocky Heads high altitude data was collected from consecutive flights, with similar surface conditions. Identifiable features are limited in both passes, so information from each was combined to establish depth processing coefficients for both data sets. An average scan line was calculated for each data set, smoothed with the 50 pixel process and applied to the appropriate data set. The final corrected deep water signal ( $V_S$ ) for Great Isaac is 113.98 in band C6 and 98.83 in band C8.

Rocky Heads required additional preprocessing to correct for sunglint effects. The procedure was similar to previous analyses. The parameters are shown in Table 12 and the improvement in data quality is illustrated in Table 13.

TABLE 12  
SUNGLINT PARAMETERS FOR ROCKY HEADS

	Band C6	Band C8
Correlation Coefficients (with C2)	0.9527	0.7742
Sunglint Correlation Coefficient	0.7922	0.4011
$(B_{ij} = \frac{\sigma_{ij}}{\sigma_{jj}})$		
Corrected Deep-water Signal ( $V_S$ )	91.99	67.3

TABLE 13  
EFFECTS OF SUNGLINT CORRECTION

	Uncorrected	Sunglint Corrected	Sunglint and Scan Angle Corrected
C6: mean = 206.15		95.59	92.00
std. dev. = 44.31		13.95	13.37
C8: mean = 130.67		75.20	68.95
std. dev. = 27.61		17.59	16.33

Bands C6 and C8 were chosen for the depth processing of both data sets. This choice was dictated by data quality and illumination conditions, as these bands were the only ones in which the signals at the depth calibration points were significantly above the deep water signal. The land editing threshold (EDL) was 254 counts and the deep water threshold (VD) was 1 count.

The low altitude Great Isaac lidar depth calibration (c.f. section 4.3) was adjusted for changes in sun elevation and applied to both (high altitude) Great Isaac and Rocky Heads.

The gain settings were constant for the different passes. The irradiance ratio is  $\frac{\sin 40^\circ}{\sin 16^\circ} = 2.33$ . Therefore  $\Delta V_L = 2.33 \Delta V_h$

for both bands. The revised depth regression equation is:

$$z = 10.783 - 1.801 \ln(\Delta V_6) + 0.921 \ln(\Delta V_8).$$

Five Great Isaac and three Rocky Heads buoys were located (Table 14), for the ship data depth processing technique. The  $\ln(\Delta V)$  was calculated for all sites, with the average deep water signal ( $V_S$ )

TABLE 14  
GREAT ISAAC AND ROCKY HEADS 10,800' RUN  
SHIP BUOYS LOCATIONS

Z	UTM-E	UTM-N	LINE	POINT	$\ln(\Delta Y)$ , C6	$\ln(\Delta Y)$ , C8	DATA SET
11.2m	687960	2877720	3272	52	2.067.	.880	Great Isaac
10.7m	689490	2877560	3728	34	2.414	.928	Great Isaac
6.6m	691310	2880020	4328	267	3.145	1.166	Great Isaac
7.2m	692000	2880330	4440	306	3.268	1.8950	Great Isaac
8.6m	692420	2879570	4472	244	2.769	1.061	Great Isaac
11.1m	735900	2860800*	2816	464	2.171	.412	Rocky Heads
8.6m	730900	2850500*	4136	362	3.577	2.705	Rocky Heads
5.1m	2846800*	732600*	4628	494	3.535	2.633	Rocky Heads

\* UTM coordinates from DECCA Navigational System before calibration was complete. The coordinates are expected to be internally consistent for each site but they may not be consistent from site-to-site or with UTM coordinates from other sources.

specific to each data set. The eight values were regressed against the respective measured depths to establish the depth coefficients to be applied to both passes. These coefficients are:  $a = 10.681$ ,  $b_1 = -4.822$ ,  $1.225$ . The correlation coefficient for depth is 0.890 with a standard error of 1.219 meters.

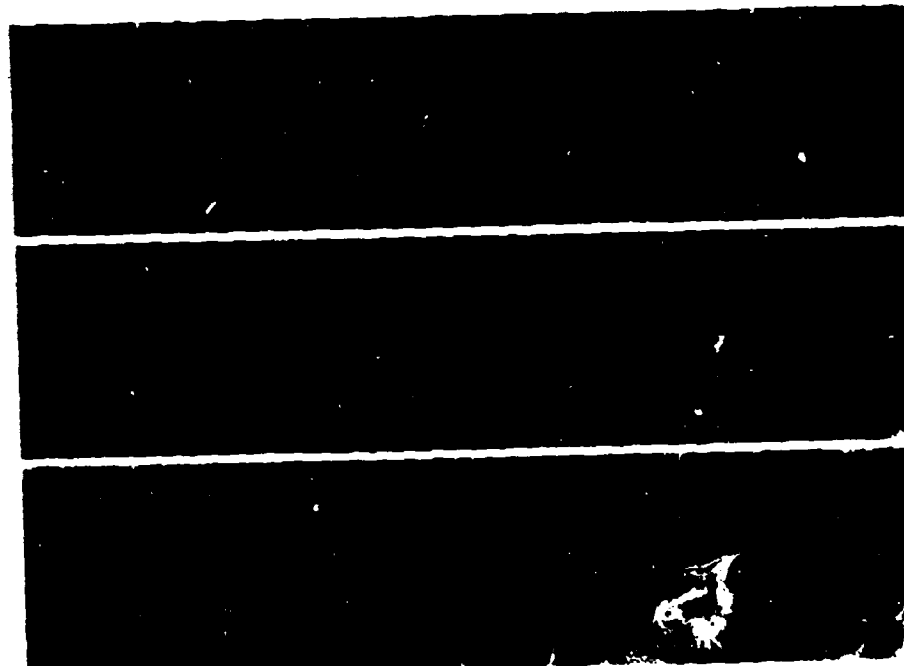
The previously determined water attenuation coefficients for C6 and C8 are  $0.146\text{m}^{-1}$  and  $0.108\text{m}^{-1}$ , respectively [5]. For the "no surface truth" depth calculations for Great Isaac and Rocky Heads, the coefficient ( $b_1$ ) is, therefore,  $b_1 = 1/2\Delta K = \pm 13.16$ .

The signal values for shallow water were extracted from data at the north end of Great Isaac Island. The thermal band A1 was used to identify land and the water depth was assumed to be 1 meter at the brightest water pixel (data record 4240, pixel 300). The depth coefficient (a) was then determined to be:

$$a = 1 + 13.16 \ln \left( \frac{237 - 114}{120 - 83} \right) = 16.809.$$

A comparison of the three depth charts is shown in Figure 20 for the Great Isaac area and in Figure 22 for the Rocky Heads area. The bottom reflectance maps for these two areas are shown in Figure 21 and 23, respectively.

**DEPTH CHART FOR THE GREAT ISAAC AREA**  
Made From Aircraft Imagery At 10,800 ft. Altitude



No Calibration

Calibrated With  
Ship Depth Data

Calibrated With  
Laser Depth Data

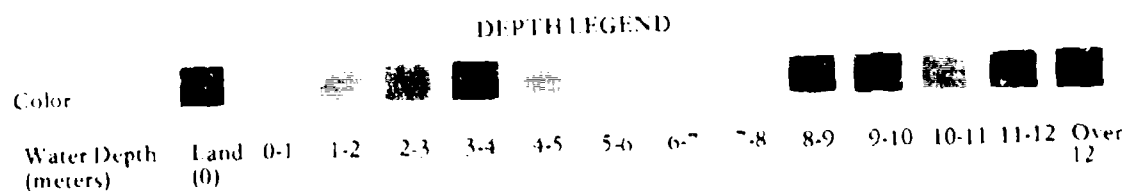


FIGURE 2C

**BOTTOM REFLECTANCE CHART  
FOR THE GREAT ISAAC AREA**

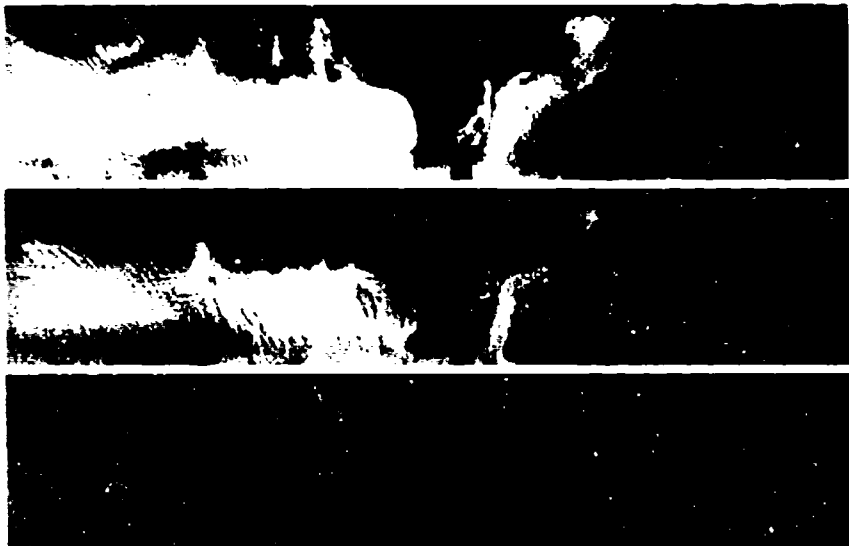
**Made From Aircraft Imagery at 10,800 ft. Altitude**



**FIGURE 21**

**DEPTH CHART FOR THE ROCKY HEADS AREA  
NORTH OF MACKIE SHOAL**

Made From Aircraft Imagery At 10,800 ft. Altitude



Calibrated With  
Laser Depth Data

Calibrated With  
Ship Depth Data

No Calibration

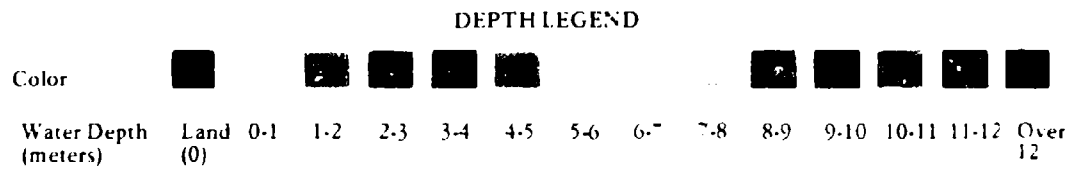


FIGURE 22

**BOTTOM REFLECTANCE CHART FOR THE ROCKY HEADS AREA  
NORTH OF MACKIE SHOAL**

**Made From Aircraft Imagery at 10,800 ft. Altitude**



**FIGURE 23**

**PRECEDING PAGE BLANK-NOT FILLED**

## ERROR ANALYSIS

Potential sources of error in the depth calculation include (1) errors in the depths used for calibration (lidar or ship soundings), (2) system noise in the multispectral scanner system, (3) fluctuations in the surface-reflected signal or path radiance, (4) changes in bottom reflectance, and (5) changes in water optical properties.

Errors in the depth measurements used for calibration may be of two kinds: first, errors in the depth values themselves, and second, errors in the location of these measurements within the multispectral scanner image. For the lidar system, the depth errors are somewhat difficult to quantify since they depend upon the method used by a human interpreter to locate the peaks of the surface-reflected and bottom-reflected pulses. One indication of the error in this process is the repeatability of the results. Experiments comparing the depths extracted by two different operators from the same data sets have shown that the results typically differ by less than 0.5 feet (0.15 m). In practice, the absolute error of the lidar depth measurement is probably limited by the sea state, since pulses striking the crest of a wave will yield a larger apparent depth than those striking the trough. A more complete discussion of lidar depth errors is given in reference [6]. Registration of the lidar depths with the passive data is maintained within one pixel by the optical alignment of the system.

For the case of calibration with shipboard depth measurements, the errors in both the magnitude of the depth and the location of the measurement relative to the multispectral scanner image are probably much greater. Although the absolute error of the depth measurement is comparable to that of the lidar measurement, the correction for tidal differences between the ship measurement and the aircraft overpass is probably not known with an accuracy better than 0.5 meters. Registration of ship measurements with the aircraft data is extremely difficult

## ERROR ANALYSIS

Potential sources of error in the depth calculation include (1) errors in the depths used for calibration (lidar or ship soundings), (2) system noise in the multispectral scanner system, (3) fluctuations in the surface-reflected signal or path radiance, (4) changes in bottom reflectance, and (5) changes in water optical properties.

Errors in the depth measurements used for calibration may be of two kinds: first, errors in the depth values themselves, and second, errors in the location of these measurements within the multispectral scanner image. For the lidar system, the depth errors are somewhat difficult to quantify since they depend upon the method used by a human interpreter to locate the peaks of the surface-reflected and bottom-reflected pulses. One indication of the error in this process is the repeatability of the results. Experiments comparing the depths extracted by two different operators from the same data sets have shown that the results typically differ by less than 0.5 feet (0.15 m). In practice, the absolute error of the lidar depth measurement is probably limited by the sea state, since pulses striking the crest of a wave will yield a larger apparent depth than those striking the trough. A more complete discussion of lidar depth errors is given in reference [6]. Registration of the lidar depths with the passive data is maintained within one pixel by the optical alignment of the system.

For the case of calibration with shipboard depth measurements, the errors in both the magnitude of the depth and the location of the measurement relative to the multispectral scanner image are probably much greater. Although the absolute error of the depth measurement is comparable to that of the lidar measurement, the correction for tidal differences between the ship measurement and the aircraft overpass is probably not known with an accuracy better than 0.5 meters. Registration of ship measurements with the aircraft data is extremely difficult

(c.f., section 3.2.3) and is probably accurate within 3-10 pixels (20-75 meters) for the high altitude data.

The effects of system noise and of fluctuations in the surface-reflected signal or path radiance remaining after the sun glint correction process (c.f. section 3.1) may be combined together for purposes of discussion. A measure of the combined system and environmental noise is the standard deviation of the deep-water signals, denoted by  $\sigma_i$  (for band i). An estimate of the depth error resulting from this source may be obtained by differentiating the depth equation with respect to the signals. Thus, a small change ( $dV_i$ ) in the band i signal results in a change in the computed depth of

$$dz = \frac{b_i}{V_i - VS_i} dV_i$$

Identifying the signal change with the "noise"  $\sigma_i$ , and assuming this noise to be uncorrelated in the various bands, the total r.m.s. depth error due to noise for a given data point having signal  $V_i$  in band i ( $i=1\dots N$ ) is

$$\Delta z = \left[ \sum_{i=1}^N \left( \frac{b_i \sigma_i}{V_i - VS_i} \right)^2 \right]^{1/2}$$

where N is the number of operating wavelength bands (2 for all cases reported here). The r.m.s. error for a given set of data points may be evaluated by substituting the actual signals into this equation. The calculated r.m.s. error can then be compared with the observed error, which may be taken as the r.m.s. difference between the lidar depths and the depths calculated from the passive data for the low altitude runs. This comparison is shown in Table 15 for the North Cat Cay and Bimini data sets. The error due to system and environmental noise appears to adequately explain the observed depth error in both cases.

TABLE 15  
COMPARISON OF CALCULATED AND OBSERVED DEPTH ERRORS  
FOR NORTH CAT CAY AND BIMINI DATA SETS

North Cat Cay:  $b_i = -4.88, 3.37$   
 $\sigma_i = 1.50, 7.26$   
 $(\Delta z)_{\text{calc}} = 0.728 \text{ meters}$   
 $(\Delta z)_{\text{obs}} = 0.708 \text{ meters}$

Bimini:  $b_i = -5.33, 1.66$   
 $\sigma_i = 4.65, 5.50$   
 $(\Delta z)_{\text{calc}} = 0.928 \text{ meters}$   
 $(\Delta z)_{\text{obs}} = 0.914 \text{ meters}$

Other possible sources of error in the depth calculation include changes in the bottom reflectance and/or water optical properties. Although the algorithm is intended to correct for these changes, it is possible that residual errors could exist because of errors in calibration or inadequacies in the correction algorithm. In order to test for residual errors associated with bottom reflectance changes, the observed error was compared with the bottom-type index which was generated independently for each scene (c.f., section 3.4). Figure 24 shows plots of the depth error ( $\Delta z$ ) and the bottom-type index ( $y$ ) versus the scan line number for the North Cat Cay scene, and Figure 25 shows a scatter plot of  $\Delta z$  versus  $y$ . No correlation is apparent in either figure, and a regression analysis indicates that the correlation coefficient for these two variables is less than  $10^{-6}$ . We may conclude that there is no significant residual error in the depth calculation due to bottom reflectance variations in this data set. This is indeed quite remarkable, since an analysis of signals at the same depth indicates that the bottom reflectance varies by at least a factor of 6 in band C5 and a factor of

$\Sigma$ ERIM

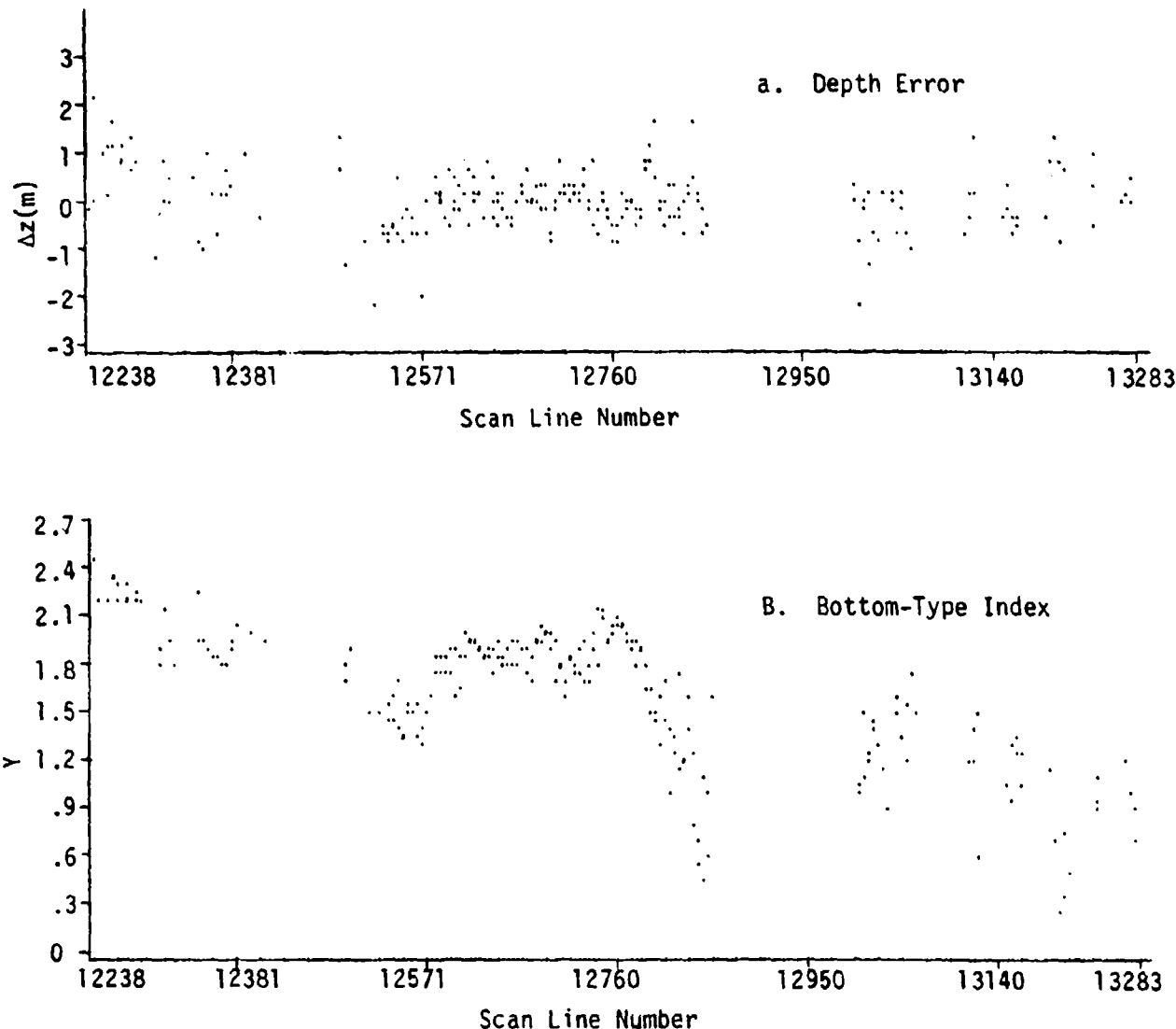


FIGURE 24. DEPTH ERROR ( $\Delta z$ ) AND BOTTOM-TYPE INDEX (Y) VERSUS SCAN LINE NUMBER FOR NORTH CAT CAY DATA SET.

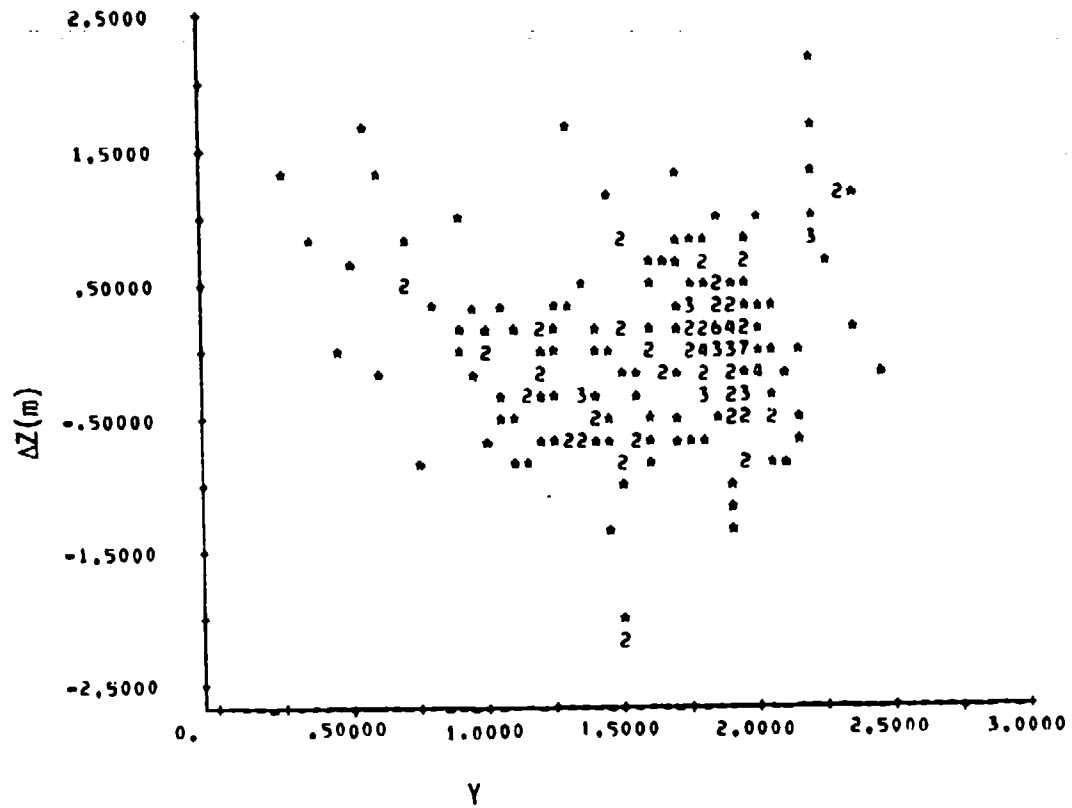


FIGURE 25. DEPTH ERROR ( $\Delta Z$ ) VERSUS BOTTOM-TYPE INDEX (Y) FOR NORTH CAT CAY DATA SET.

16 in band C8. Although no direct information on water parameter variations is available, the absence of any apparent systematic depth error (c.f. Figure 24) and the close agreement between the observed r.m.s. depth error and the calculated error due to noise seems to rule out the existence of residual errors due to water parameter variations as well.

Plots of the depth error and the bottom-type index for the Bimini data set are shown in Figures 26 and 27. There appears to be some systematic depth error near the shoreline (left side of Figure 26), but Figure 27 does not indicate any significant correlation with the bottom reflectance (the correlation coefficient for  $\Delta z$  and  $y$  is 0.00372). Thus, it seems likely that this error is caused by water attenuation variations near the shoreline. Another possibility is that there is some miscalibration in this data set, because the majority of the depth samples are in the 8-10 meter range, with a relatively small number of calibration points below 6 meters. The regression analysis may thus have minimized the error in the 8-10 meter range while allowing a greater error for the shallow points. In the future, it is suggested that the calibration depths be sampled to represent the entire range of depths more evenly.

For the high altitude data sets, insufficient surface truth information exists to carry out a detailed error analysis. However, in view of the apparent success of the error calculation involving only system and environmental noise in explaining the observed error for the low altitude cases, a similar calculation may be used to estimate the errors for the high altitude data. In order to estimate the r.m.s. depth error for a given scene, the distribution of signals must be known. This may be obtained from a histogram of the scene; however, in order to obtain analytical results it will be assumed here that the signals are distributed uniformly from the minimum value ( $V_{MIN_i}$ ) above the threshold described in section 3.3 to the maximum value ( $V_{MAX_i}$ ) observed in the scene. This assumption implies an exponential depth distribution which is weighted more heavily toward the shallower depths. This would be

$\Sigma$ ERIM

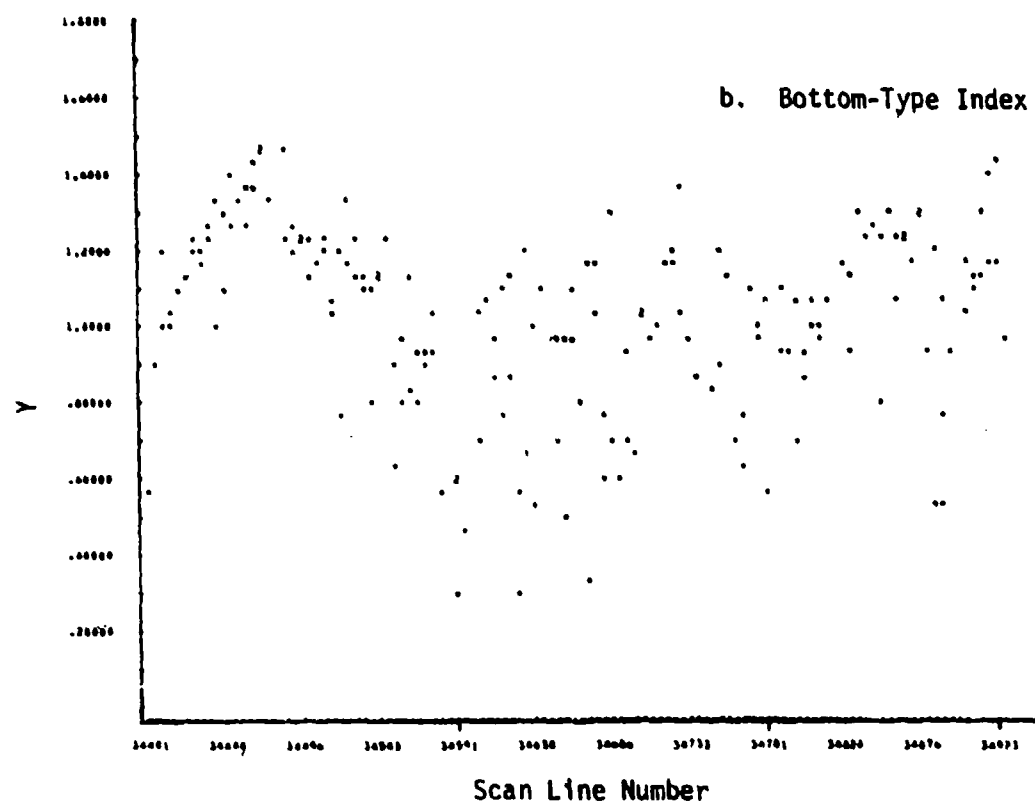
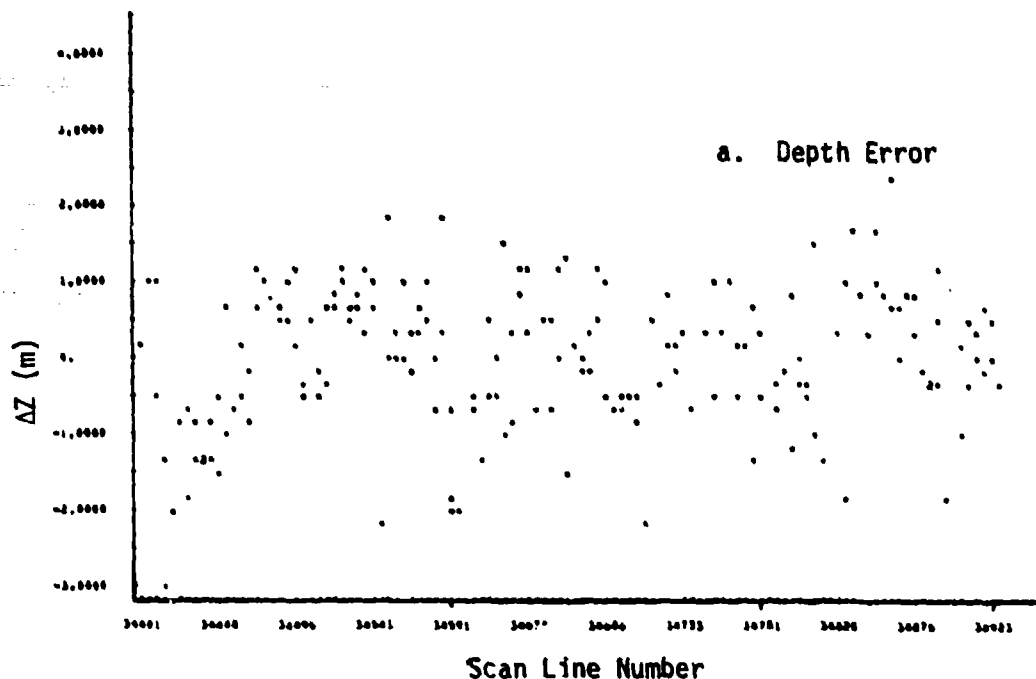


FIGURE 26. DEPTH ERROR ( $\Delta Z$ ) AND BOTTOM-TYPE INDEX (Y) VERSUS SCAN LINE NUMBER FOR BIMINI DATA SET.

$\Sigma$ ERIM

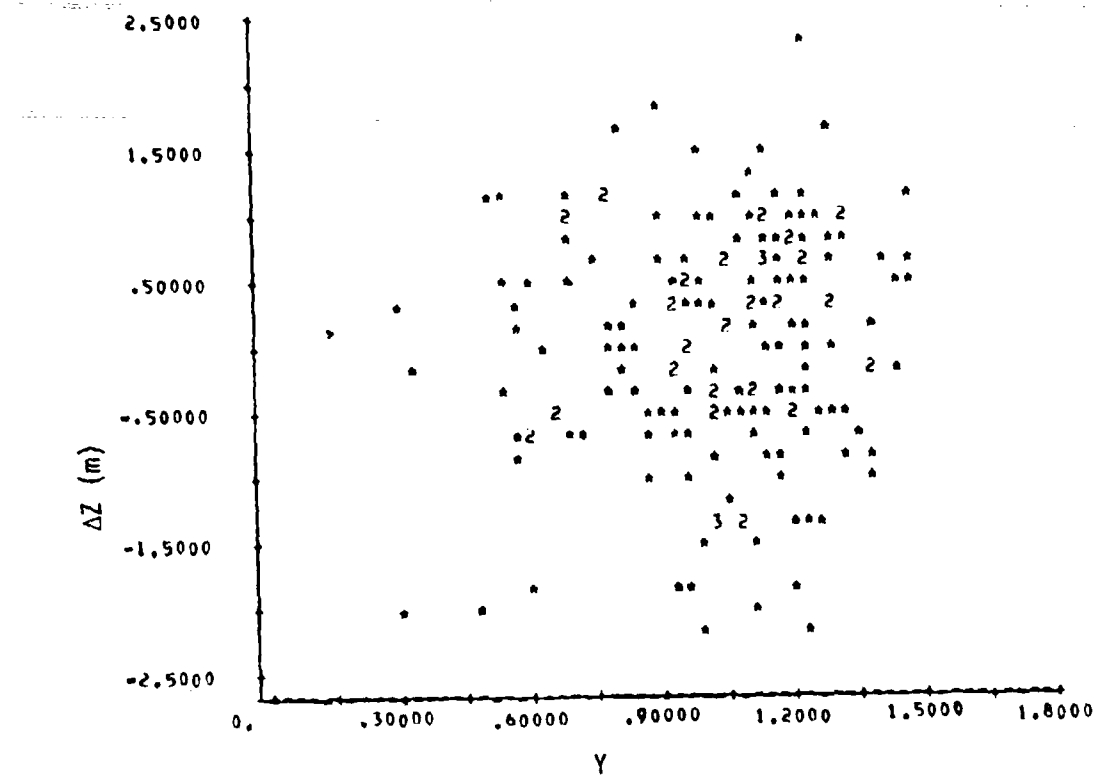


FIGURE 27. DEPTH ERROR ( $\Delta Z$ ) VERSUS BOTTOM-TYPE INDEX ( $Y$ ) FOR BIMINI DATA SET.

representative of a situation similar to that in the Bahamas where there are extended areas of shallow water with a fairly abrupt transition to deeper water. The mean-square error for a scene containing a signal distribution  $P(V_i)$  is

$$(\Delta z)^2 = \sum_{i=1}^N \int P(V_i) \left( \frac{b_i \sigma_i}{V_i - VS_i} \right)^2 dV_i.$$

Therefore, for a uniform distributions of signals

$$P(V_i) = \begin{cases} \frac{1}{VMAX_i - VMIN_i} & \text{for } VMIN_i < V_i < VMAX_i \\ 0 & \text{otherwise} \end{cases}$$

The mean-square error is

$$\begin{aligned} (\Delta z)^2 &= \sum_{i=1}^N \frac{1}{VMAX_i - VMIN_i} \int_{VMIN_i}^{VMAX_i} \left( \frac{b_i \sigma_i}{V_i - VS_i} \right)^2 dV_i \\ &= \sum_{i=1}^N \frac{(b_i \sigma_i)^2}{(VMIN_i - VS_i)(VMAX_i - VS_i)} \end{aligned}$$

where  $N$  is the number of wavelength bands used for processing. The values of  $\sigma_i$ ,  $VMIN_i$ , and  $VMAX_i$  are shown in Table 16 for each high altitude scene processed, along with the calculated depth errors for the lidar calibration case. For the other two calibration methods it is expected that errors due to miscalibration and residual errors due to bottom reflectance and/or water parameter changes will dominate.

TABLE 16  
CALCULATED DEPTH ERRORS FOR  
HIGH ALTITUDE DATA SETS

1. North Cat Cay (Run 5, 8/12/78, 0900)

$$b_i = -6.37, 5.46$$

$$\sigma_i = 2.50, 3.01$$

$$V_{MIN_i} - V_{S_i} = 5.02, 5.71$$

$$V_{MAX_i} - V_{S_i} = 202.02, 154.71$$

$$\Delta z = 0.75 \text{ meters}$$

2. Bimini (Run 7, 8/12/78, 0900)

$$b_i = -5.33, 1.66$$

$$\sigma_i = 2.87, 2.40$$

$$V_{MIN_i} - V_{S_i} = 3.05, 3.56$$

$$V_{MAX_i} - V_{S_i} = 128.05, 56.56$$

$$\Delta z = 0.82 \text{ meters}$$

3. Great Isaac and Rocky Heads (Run 10 and 12, 8/12/80, 1600)

$$b_i = -1.80, 0.92$$

$$\sigma_i = 8.64, 4.35$$

$$V_{MIN_i} = 1.00, 1.00$$

$$V_{MAX_i} = 123.00, 37.00$$

$$\Delta z = 1.55 \text{ meters}$$

It may be noted, by comparison of Tables 15 and 16, that the calculated depth errors are comparable for the low and high altitude cases, and in fact the high altitude Bimini data set shows a slightly smaller  $\Delta z$  than the low altitude case. It should be remembered, however, that the values in Table 15 are for a specific set of points whereas those in Table 16 are average values based on the assumption of a uniform distribution of signals. If this same assumption is made for the low altitude data sets one obtains slightly smaller depth errors of 0.64 meters for North Cat Cay and 0.66 meters for Bimini. The actual dependence of the

depth error on altitude requires further study, and no definite conclusions can be made at this time. There appear to be counterbalancing effects in that the environmental noise (due to surface fluctuations) decreases with altitude while the signal level also decreases due to atmospheric attenuation. Whether there is a net increase or decrease in the depth error with altitude depends on the relative magnitude of these effects, which is not yet well known.

## CONCLUSIONS

The results of the various depth extraction processing methods can be summarized as follows.

- (1) Preprocessing steps must be applied to airborne multispectral data before reliable depths can be extracted because of the wide angle ( $90^\circ$ ) coverage of an airborne scanner. Sunglint removal is accomplished best by using the nonpenetrating near infrared channel to approximate the surface reflection and subsequently adjusting the green band signal. Despite the smaller total view angle, similar preprocessing procedures are recommended for seasonal spaceborne data collected at certain latitudes under sun elevations and sea state conditions that could produce the necessity for sunglint removal from the data set.
- (2) Depth charts using laser time difference signals as the source of calibration points provided the most accurate depth measurements when extrapolated to the passive multispectral scanner data. Depths were known more accurately geographically in comparison with ship data because of problems with the Decca navigation network. Depending on the data set and signal quality depth error ranged from 0.7 meter for the North Cat Cay site to 0.9 meter for the Bimini Island site.
- (3) Although the r.m.s. difference between the lidar measurement of depth and the scanner depth is larger than the expected error in the laser depths, this difference appears to be due mostly to noise in the multispectral scanner data. Since this noise can be reduced by improved system design, the technique of using multispectral scanner data to extrapolate the laser

depths to a larger area for every picture element seems to be valid and practical.

- (4) Bottom reflectance variations do not adversely affect this extrapolation and water quality changes have not appeared to cause large errors in this investigation although they may cause problems in more turbid coastal waters. No significant residual error in the depth calculation due to bottom reflectance variations was noted for the North Cat Cay data set, despite variances of reflectance by factors of 6 and 16 in the respective spectral channels. Close agreement was found between the observed r.m.s. depth error and the calculated error due to noise thus suggesting no residual errors due to water parameter variations as well.
- (5) The calculated depth errors are comparable for the low and high altitude sites ranging from .75 meter at North Cat Cay, .82 meter at Bimini, and 1.55 meters at Great Isaac. The Great Isaac site had fewer control points and poorer signal quality. The dependence of the depth error on altitude requires further analysis especially in relating the decrease in environmental noise due to surface reflections as a function of altitude to the decrease in signal level due to higher atmospheric attenuation to see which dominates.

## REFERENCES

1. E. Doak, J. Livisay, D. Lyzenga, J. Ott, and F. Polcyn, Evaluation of water depth extraction techniques using Landsat and aircraft data, ERIM Report No. 135900-2-F, January 1980.
2. D. Lyzenga and J. Livisay, Documentation of computer software for multispectral bathymetry analysis, ERIM Report No. 148900-1-F, April 1980.
3. D.R. Lyzenga, Passive remote sensing techniques for mapping water depth and bottom features, Applied Optics 17, 379-383 (1978).
4. D.R. Lyzenga, Shallow water reflectance modeling with applications to remote sensing of the ocean floor, Proceedings of 13th International Symposium on Remote Sensing of Environment, 583-602 (1979).
5. D.R. Lyzenga, Coastal remote sensing investigations, Volume 1: Marine Environment, ERIM Report No. 134400-11-F, April 1980.
6. G.C. Guenther and L.R. Goodman, Laser Applications for Near-Shore Nautical Charting, SPIE 160. Ocean Optics V, 174-183 (1978).

DISTRIBUTION LIST

Headquarters, Defense Mapping Agency (Copy 1, 2)  
(Attn: Code STT, CDR V. K. Nield, A. Krygiel)  
U. S. Naval Observatory, Building 56  
Washington, DC 20305

Defense Mapping Agency Hydrographic/Topographic Center (Copy 3, 4)  
(Attn: Code STT, R. Sinclair, J. Hammack)  
6500 Brookes Lane  
Washington, DC 20315

Naval Ocean Research and Development Activity (Copy 5, 6)  
(Attn: Code 550, C. Crandall, M. Houck)  
NSTL Station MS 39529

Naval Research Laboratory (Copy 7, 8)  
(Attn: NRL 7006, Dr. V. Noble; Code 7912, P. Mitchell)  
Washington, DC 20375

Naval Oceanographic Office (Copy 9, 10)  
(Attn: Code 3540, L. Borquin; Code 3500, R. Higgs)  
NSTL Station, MS 39522

Chief of Naval Operations (Copy 11, 12)  
(Attn: OP952D, CDR John Chubb; OPNAV 372E, CDR McCurdy)  
Washington, DC 20350

Commander, Naval Oceanography Command (Copy 13)  
(Attn: Code N56, R. H. Evans)  
NSTL Station  
Bay St. Louis, MS 39529

Rome Air Development Center (Copy 14, 15)  
RADC/ISCA  
(Attn: D. F. Trad)  
Griffiss AFB, NY 13441

Headquarters, Naval Material Command (Copy 16, 17)  
(Attn: NAVMAT 0724, CAPT E. Young, USN  
NAVMAT 07M, LCOL G. Gay)  
Washington, DC 20360

Director, Development Center (Copy 18)  
Marine Corps Development and Education Center  
(Attn: Intelligence Div., CAPT E. D'Antonio, USMC)  
Quantico, VA 22134

Naval Air Systems Command  
(Attn: NAVAIR 370P, T. Czuba; NAVAIR 548, L. Wheat)  
Washington, DC 20361

(Copy 19, 20)

Office of Naval Research  
(Attn: ONR 462, J. Bailey, ONR 486, M. Blizzard)  
Arlington, VA 22217

(Copy 21, 22)

Director  
Defense Technical Information Center  
Cameron Station  
Alexandria, VA 22314

(Copy 23, 24)

Environmental Research Institute of Michigan  
(Attn: F. Thomson, D. Lyzenga, J. S. Ott,  
J. Livisay, F. Polcyn)  
P. O. Box 8618  
Ann Arbor, MI 48107

(Copy 25, 25,  
27, 28, 29)

National Ocean Survey  
Engineering Development Laboratory (C61)  
(Attn: D. Enabnit, G. Guenther)  
NOAA/NOS  
Rockville, MD 20852

(Copy 30, 31)

Naval Environmental Prediction Research Facility  
(Attn: A. Weinstein)  
Monterey, CA 93940

(Copy 32)

Commander  
Naval Ocean Systems Center  
(Attn: Code 8105, D. Leonard)  
San Diego, CA 92152

(Copy 33)

Officer-in-Charge  
Naval Facilities Engineering Command Detachment  
Civil Engineering Laboratory  
(Attn: T. Foresman)  
Naval Construction Battalion Center  
Port Huaneme, CA 93043

(Copy 34)

Director  
Hawaii Laboratory  
Naval Ocean Systems Center  
(Attn: Code 722, M. Fielding)  
P. O. Box 997  
Kailua, HI 96734

(Copy 35)

Goddard Space Flight Center  
(Attn: Earth Resources Branch, Dr. C. Schnetzler)  
Greenbelt, MD 20771

(Copy 36)

NOAA/NESS  
(Attn: Mr. J. W. Sherman III)  
Washington, DC 20233

(Copy 37)

National Ocean Survey  
(Attn: Code C34, CDR Simmons)  
Chief, Photogrammetry Division  
NOAA/U. S. Department of Commerce  
6001 Executive Blvd.  
Rockville, MD 20852

(Copy 38)

U. S. Geological Survey  
(Attn: A. P. Colvocoresses)  
National Center, Stop 522  
Reston, VA 22092

(Copy 39)